Applied Thermal Engineering 278 (2025) 127128

Contents lists available at ScienceDirect

Applied Thermal Engineering

journal homepage: www.elsevier.com/locate/apthermeng

Research Paper

Dropwise-to-filmwise transition during condensation of steam on hydrophilic surfaces☆

Marco Tancon [a,*], Antonio Abbatecola [a], Stefano Bortolin [a], Lorenzo Facco [a,b], Riccardo Parin [b], Davide Del Col [a]

[a] Department of Industrial Engineering, University of Padova, Via Venezia 1, 35131 Padova, Italy
[b] TerraXcube, Eurac Research, Via Ipazia 2, 39100 Bolzano, Italy

ARTICLE INFO

Keywords:
Dropwise condensation
Heat transfer
Hydrophilic surface
Numerical modeling
Transition
Droplet removal

ABSTRACT

Dropwise condensation (DWC) is a two-phase heat transfer process that is expected to achieve heat transfer coefficients (HTCs) several times higher as compared to filmwise condensation (FWC). Usually, low-wettability coatings are required to promote DWC on metallic surfaces. However, recent studies suggest that hydrophilic (wettable) surfaces with low contact angle hysteresis can further increase the heat transfer coefficient, potentially leading to heat transfer processes with higher effectiveness. Despite this potential, the ability of such surfaces to sustain enhanced DWC without flooding remains unclear. Moreover, the underlying mechanisms governing the transition from DWC to FWC, which is likely to occur on hydrophilic surfaces, remain poorly understood. While some studies have addressed this phenomenon, conclusive findings are still lacking.

This paper aims to address these unclear aspects of DWC by investigating pure steam condensation on samples with varying wettability at a constant saturation temperature (107 °C) while adjusting the coolant medium temperature from 20 °C to 95 °C. Heat transfer measurements and high-speed imaging were employed to provide a detailed analysis of how the saturation-to-wall temperature difference, and consequently heat flux, affects the condensation mode. The results demonstrate that DWC can be effectively sustained on hydrophilic surfaces with enhanced droplet mobility, achieving HTC values up to 70 % higher than those observed for DWC on hydrophobic surfaces. However, on hydrophilic surfaces, the transition from DWC to FWC occurs at lower wall subcooling values. As a further step, a simplified model for predicting the condensation mode and the heat flux during DWC is proposed and validated using the present experimental data. The model is found to accurately predict the effect of surface wettability and subcooling on the dropwise condensation HTC, with a mean deviation between calculated and measured values lower than 12 %. Furthermore, the model enables the successful identification of the subcooling range over which DWC can be sustained, based on the surface properties and operating conditions.

1. Introduction

Dropwise condensation (DWC) is a phase-change process that involves the formation and rapid removal of randomly distributed drops on the condensing surface. It is well-established that promoting DWC can significantly improve the heat transfer performance as compared to filmwise condensation (FWC) [1,2]. The condensation mode, whether FWC or DWC, is determined by the operating conditions, such as heat flux, saturation temperature, and vapor velocity as well as the interaction between the condensing fluid and the surface. The latter is typically characterized by surface wettability, which is macroscopically evaluated through contact angle measurements.

To promote DWC on metallic surfaces, low surface energy coatings are needed, indeed hydrophobic coatings (static contact angle ~90°) are usually employed [3–5]. Recent studies have suggested that DWC on hydrophilic surfaces with low contact angle hysteresis can provide additional advantages such as reduced thermal resistance associated with conduction through the droplets [6], enhanced nucleation [7], facilitated sweeping [8], and thus higher heat transfer coefficients (HTC) [9,10]. However, owing to the challenges in surface coating realization,

---

☆ This article is part of a special issue entitled: 'Conference ExHFT-10' published in Applied Thermal Engineering.

* Corresponding author.

E-mail address: marco.tancon@unipd.it (M. Tancon).

https://doi.org/10.1016/j.applthermaleng.2025.127128
Received 21 December 2024; Received in revised form 8 May 2025; Accepted 4 June 2025

there is a lack of measurements dealing with DWC of pure steam on hydrophilic surfaces with low contact angle hysteresis, and the actual advantage of promoting DWC on such surfaces is still unclear.

Another aspect that is still poorly understood is the transition from dropwise to filmwise condensation, which is likely to occur on hydrophilic surfaces. The ratio of DWC heat transfer coefficient to FWC heat transfer coefficient can be close to 10 [11,12], hence identifying the key parameters (e.g. wall subcooling, surface characteristics, fluid properties) involved in the transition from DWC to FWC and understanding their role in the condensation process is fundamental. Although Stylianou and Rose [13] and Utaka et al. [14,15] conducted studies to clarify the transition mechanism, no definitive conclusions were drawn.

The transition could be linked to one or both of the following mechanisms [13]. Firstly, for sufficiently high wall subcooling, the rate at which new portions of the surface are cleaned by coalescence and sweeping events becomes unable to sustain the increasing condensation rate. Secondly, considering that the radius of the smallest thermodynamically viable drop is inversely proportional to the subcooling, increasing the saturation-to-wall temperature difference activates smaller nucleation sites, potentially resulting in the formation of a continuous film. Nevertheless, it is accepted that DWC can only be maintained up to a certain value of subcooling and heat flux, which is strongly dependent on surface properties and operating conditions [16,17]. Despite these hypotheses, the fundamental understanding of the mechanisms responsible for the transition from DWC to FWC remains a significant and unresolved challenge in the field.

Complete condensation curves, covering all condensation modes from DWC to FWC, have been mainly measured for fluids with low surface tension (such as propylene glycol, ethylene glycol, glycerol) that condense on polytetrafluoroethylene (PTFE) or oleic acid coated surfaces [10,14,15,18]. The aforementioned studies have yielded values of peak heat flux (before the transition to FWC) in the range 500–1000 kW m^{-2}, depending on the specific pair vapor-surface. Despite the considered surfaces being hydrophobic with water (equilibrium contact angle $\theta_e \geq 90^\circ$), their behaviour could have turned into highly wettable ($\theta_e < 90^\circ$) with reduced contact angle hysteresis when the condensing vapor has a lower surface tension (e.g., $\sigma_{prop,\ glycol} = 39$ mN m^{-1} at 20 °C) compared to water (e.g., $\sigma_{water} = 73$ mN m^{-1} at 20 °C) [19], resulting in a condensation behaviour similar to that of steam on hydrophilic surfaces with low contact angle hysteresis. To the best of the authors' knowledge, only Takeyama and Shimizu [20] documented the DWC/FWC transition using pure steam as condensing fluid. Their findings indicated that the heat flux peak for the transition occurs at values above 7 MW m^{-2}.

The present study aims to address the existing gaps in the literature regarding the ability of hydrophilic surfaces to promote and sustain DWC. It will be demonstrated that, according to the operating conditions, hydrophilic surfaces with sufficiently high droplet mobility can sustain DWC, overperforming classical hydrophobic surfaces in terms of HTC. Additionally, this study will contribute to advance the understanding of the mechanisms governing the transition from DWC to FWC and vice versa.

To achieve these objectives, sol–gel coated aluminium samples with hydrophilic behaviour (advancing contact angle, θ_a, below 70°) and reduced contact angle hysteresis ($\Delta\theta < 25^\circ$) were tested during DWC of pure steam at constant saturation temperature ($T_{sat} = 107$ °C). Tests at variable coolant inlet temperature (20–95 °C) were performed to assess the effect of wall subcooling and heat flux on the DWC phenomenon and HTC. To support the heat transfer data and provide a clear description of the DWC/FWC transition, high-speed videos of the phenomenon were recorded and analysed to characterise the evolution of the condensation mode. Furthermore, a key novelty of this work is the development of a simplified numerical method to predict both the DWC heat flux and the range of surface subcoolings over which a functionalized surface can sustain DWC. To the best of the authors' knowledge, no similar calculation methods are currently available in the literature. Overall, the findings of this study represent a significant step forward for both the practical applications of DWC and the theoretical understanding of the phenomenon.

2. Materials and methods

2.1. Sample fabrication and characterization

In this study, DWC of steam is investigated on two different aluminium sol–gel coated substrates having a condensation area of 50 mm × 20 mm. Samples are made of 6082 aluminum alloy, mirror-

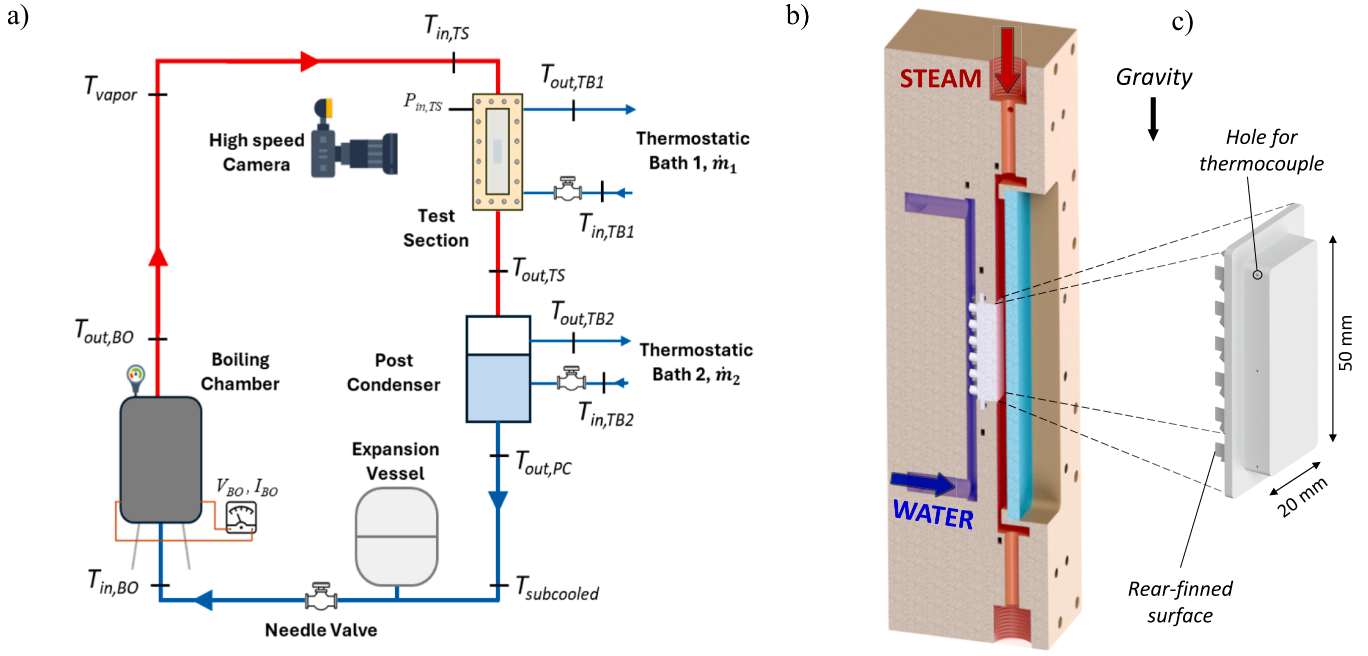

Fig. 1. Experimental apparatus. a) Layout of the thermosyphon loop. b) 3D section view of the test section. c) 3D model of the tested sample with dimensions (in mm). The gravity direction is shown.

polished on the condensation side before the deposition of the coating. The substrate was functionalized with a sol–gel silica film obtained by acid catalyzed hydrolysis and condensation of TEOS (tetraethylorthosilicate), MTES (methyltriethoxysilane), OTES (octyltriethoxysilane) in alcoholic media. The solution was prepared by mixing TEOS, MTES, OTES, EtOH, HCl 1 M and H2O in molar ratios of (TEOS + MTES + OTES):EtOH:HAc:HNO3 (0.1 M) = 1:0.01:2.9:150 respectively, with molar fractions of silane precursors TEOS:MTES:OTES = 0.35:0.6:0.05. The deposition process was performed under controlled air humidity (25 %) by dip-coating the aluminum substrates into the prepared solution at a withdrawal speed of 12 cm min^{-1}. Post-deposition, the samples underwent heat treatment in air within a furnace for 1 h. Depending on the temperature of the heat-treatment, either 450 °C or 300 °C, two different samples were obtained, named MTO-450 and MTO-300, respectively.

Fourier-Transform Infrared (FTIR) spectroscopy was employed to investigate the presence of organic hydrophobic groups on the developed coatings. Measurements were conducted in the 400–4500 cm^{-1} range using a Jasco FT-IR 690 in ATR (Attenuated Total Reflectance) mode. The thickness of sol–gel films was evaluated by using a J.A. Woollam V VASE® Spectroscopic Ellipsometer at three different angles of incidence (50°, 60°, 70°) in the wavelength range 300–1200 nm. Optical micrographs of the samples were collected with a Leica® DMRE optical microscope.

The wettability of the surfaces was evaluated by measuring the advancing (θ_a) and receding (θ_r) contact angles through the standard sessile drop method. This involved recording a water droplet's quasi-static expansion and contraction over a horizontal surface. Videos captured using a compact CMOS camera (Thorlabs® model DCC1545M, Bergkirchen, Germany) with a zoom lens (Thorlabs® model MVL7000, Bergkirchen, Germany) were analyzed through an in-house Matlab® code to automatically evaluate the contact angles from the images. For each surface, the contact angles were determined before and after condensation tests considering the average of eight measurements on eight different positions on the sample. The corresponding standard deviation was considered representative of the experimental uncertainty and was therefore used as an indicator of the uniformity of surface wettability.

Since the adhesion of volatile organic compounds (VOCs) to the surface has been demonstrated to modify contact angles [21,22], a series of measures have been adopted to minimize the effects of VOC contamination. Firstly, the coated samples were fabricated ~24 h before testing and stored in sealed conditions to prevent any exposure to ambient contaminants prior to condensation. Secondly, the surface wettability was evaluated immediately before and after each condensation experiment. Thirdly, tests were performed in a pure steam environment, using high-purity distilled water, and the system was operated under a slight overpressure, removing all non-condensable gases (NCGs) prior to testing. Finally, only inert materials (stainless steel tubing and a PEEK) were employed to eliminate any source of organic contaminants from the apparatus itself.

2.2. *Experimental setup for condensation tests*

The experimental campaign was conducted using the test rig schematized in Fig. 1a. The setup is a thermosiphon loop made of three main components: a boiling chamber, a test section, and a post-condenser. Complete details regarding the components of the test rig can be found in [23,24]. Briefly, steam is initially generated within the boiling chamber, which houses two electric resistances with total power of 6 kW. From the boiling chamber, the steam flows into the test section, where it partially condenses on the specimen cooled by a thermostatic bath. At the exit of the test section, the two-phase mixture completes the condensation process within a post-condenser. Finally, the subcooled liquid exiting the post-condenser returns to the boiling chamber. The fluid motion in the loop is due to different density of the fluid in the liquid and vapor lines.

The boiling chamber and the test section are connected by a stainless-steel tube around which an electric resistance is wrapped to ensure the presence of superheated steam (~4 K) and the absence of liquid droplets at the test section inlet. Although this study was conducted with a constant steam velocity, it is noteworthy that by varying the power in the boiling chamber, tests can be performed at different steam velocities, up to a maximum value of about 14 m s^{-1} as discussed in Tancon et al. [25,26].

Non-condensable gases can significantly hinder heat transfer during DWC. To address this issue, the vapor is vented multiple times through two discharge valves: one at the top of the circuit and the other in the upper section of the post-condenser. This repeated venting, while the apparatus reaches stable operating conditions, effectively eliminates any NCGs dissolved in the water. Additionally, the apparatus is operated under overpressure to further minimize NCG presence and is regularly vacuumed before being filled with deionized water.

The test section (Fig. 1b), made of PEEK, is the core of the experimental apparatus. It allows for both heat transfer measurements and simultaneous visualization of the phenomenon through a glass window. The aluminum sample is positioned inside the test section. Each specimen is designed with six thermocouple insertion holes, three on each side of the sample, located at two different depths from the coated surface ($z_1 = 1.3$ mm and $z_2 = 2.8$ mm). Consequently, six thermocouples are embedded in each sample, and are used to evaluate the local surface temperatures ($T_{wall,j}$) of the sample at three longitudinal positions along the flow direction (inlet, middle, and outlet).

The back of the specimen, opposite the condensation side, is machined to obtain a finned surface. In fact, the thermal resistance on the water side is about one order of magnitude higher than the DWC thermal resistance and the maximum temperature difference between steam and cooling water is limited by the saturation pressure inside the test section and by the freezing temperature of the coolant (water). Machining fins on the back side of the specimen leads to a reduction of the heat transfer resistance and consequently extends the heat flux range that can be investigated. The finned surface has a double effect: it enhances the convective HTC thanks to the continuous disturbance of the boundary layer and, at the same time, increases the heat transfer area. As presented in Tancon et al. [27], the surface of the sample designed on the coolant side consists of an array of fins having a square cross-section (2 × 2 mm^2), inclined by 45° with respect to the water flow direction: fins height is equal to 4 mm and fins pitch is equal to 3 mm. The 3D model of the sample is shown in Fig. 1c.

For the visualization of the condensation process, a setup comprising a high-speed camera (Photron® FASTCAM Mini UX100, Tokyo, Japan) coupled with a macro lens (TOKINA®) was utilized. The illumination system consists of a single powerful LED. All videos were recorded at a high frame rate (1250 fps) and a resolution of 1280 by 1024 pixels. This configuration allows for recording videos that can be used to evaluate both the maximum droplet radius and the drop-size distribution.

2.3. *Data reduction and experimental procedure*

To characterize the heat transfer performance during condensation, it is essential to evaluate the heat transfer coefficient (HTC). This can be accomplished by applying Eq. (1):

$$\mathrm{HTC} = q/\Delta T_{sub} \tag{1}$$

where q is the average heat flux during DWC, and ΔT_{sub} is the saturation-to-wall temperature difference.

The parameter q is determined from a thermal balance on the coolant side of the test section, as expressed in Eq. (2):

$$q = \dot{m}_w \, c_w \, \Delta T_w / A \tag{2}$$

In Eq. (2), ΔT_w represents the temperature rise of the coolant

Table 1
Range of variation for the main parameters measured during the experimental campaign with corresponding average uncertainty.

Quantity	MTO-300	MTO-450	Avg. uncertainty
Absolute pressure [bar]	1.28	1.28	±0.1 %
Saturation temperature [°C]	107	107	±0.5
Avg. vapor inlet velocity [m s^{-1}]	3.5	3.5	± 0.2
Coolant mass flow rate [kg s^{-1}]	0.10	0.10	±1 %
Coolant inlet temperature [°C]	20–90	20–95	±0.05
Coolant temperature difference [K]	0.4–1.4	0.5–2.1	±0.03
Heat flux [kW m^{-2}]	150–850	130–600	±4 %
HTC [kW m^{-2} K^{-1}]	60–140	15–175	±6 %

between the inlet and outlet of the test section, $\dot{m}_w$ is the coolant mass flow rate, c_w is the specific heat capacity of the coolant, and A is the area of the condensing surface (50 mm × 20 mm). The accuracy of this measurement is verified by comparing the results obtained from Eq. (2) with the average heat flux determined by applying Fourier's law to the three thermocouple pairs embedded in the metallic substrate. For the present experimental data, the discrepancy between the two methods is less than 8 % when the average heat flux is higher than 300 kW m^{-2}.

The mean saturation-to-wall temperature difference over the condensing surface (which is also called surface subcooling) is calculated by averaging three local subcooling values measured along the flow direction ($T_{sat} - T_{wall,j}$), as follows:

$$\Delta T_{sub} = \sum_{j=in}^{out} \frac{\left(T_{sat} - T_{wall,j}\right)_j}{3} \tag{3}$$

where the saturation temperature T_{sat} is obtained from the value of saturation pressure measured at the test section inlet corrected by considering the frictional pressure drop between the pressure port location and the given cross section in the channel [26]. While the local surface temperatures $T_{wall,j}$ at the three different locations (inlet, middle and outlet) are obtained applying the Fourier law (Eq. (4)) to the thermocouples' readings considering a thermal conductivity (λ_{al}) of the 6082 aluminum alloy equal to 180 W m^{-1} K^{-1}.

$$T_{wall,j} = T_{z_1\,j} + q\ z_1/\lambda_{al} \tag{4}$$

It is important to note that, since Eqs. (3) and (4) are used to evaluate the temperature difference between the saturation temperature and the substrate temperature just below the promoter layer, the HTC calculated by Eq. (1) accounts for both the condensation thermal resistance and the conduction resistance through the sol–gel coating.

As previously mentioned, by acting on the power of the boiling chamber, it is possible to vary the vapor velocity at the inlet of the test section. Knowing the power supplied to the electrical resistances (Q_{BO}) and applying an energy balance to the boiling chamber, it is possible to calculate the mass flow rate circulating in the system ($\dot{m}_v$). By dividing $\dot{m}_v$ for the cross-section of the channel ($S_v = 5$ mm × 30 mm), the mass flux (G_v) is determined. Finally, the vapor velocity at the inlet of the test section (v_v) can be evaluated according to the following equation:

$$v_v = \frac{G_v}{\rho_v} = \frac{Q_{BO}}{(h_v - h_{ls})\rho_v\ S_v} \tag{5}$$

In Eq. (5), h_v is the vapor enthalpy obtained from the saturation pressure reading, h_{ls} is the enthalpy of the subcooled liquid evaluated from the thermodynamic conditions at the inlet of the boiling chamber, ρ_v is the vapor density in saturated conditions. To ensure enough vapor to condense even at the highest heat flux, the power supplied to the boiling chamber for these tests was set at 1 kW, which corresponds to an average inlet vapor velocity of about 3.5 m s^{-1}.

The experimental campaign was conducted on two samples with different wettability, maintaining a constant saturation temperature (107 °C) and a low steam velocity (3.5 m s^{-1}), while varying the temperature of the cooling water entering the test section. All operating conditions are summarized in Table 1. Each experimental point presented in this paper was obtained as the average of 480 measurements taken at a frequency of 1 Hz. The main parameters underwent to uncertainty analysis in accordance with the ISO guide, considering a coverage factor $k = 2$ for the evaluation of combined uncertainties.

The data acquisition system includes the sensors (e.g., pressure, temperature and flow rate transducers), signal wirings, a DAQ (data acquisition) device (National Instruments SCXI-1102 with PCI 6034E), and a computer. Furthermore, an ice-point reference was used to maintain the cold junction of the thermocouples at zero degrees Celsius ± 0.02 °C. To ensure accurate heat transfer measurements, the temperature sensors (with the entire measurement chain) were calibrated using a Fluke® 1586A Super-DAQ precision data logger in combination with a Pt100 platinum resistance thermometer over the 60–100 °C range and two AS115 four-wire thermistor probes over the 20–60 °C interval. This high-precision data logger has an accuracy of ±0.005 K when using the AS115 probe and of ±0.01 K when using the Pt100 probe. By comparing thermocouples' readings with reference probes, a linear calibration function has been found for each thermocouple that corrects the reference equation for T-type thermocouples given by NIST. After the calibration procedure, the deviation between the thermocouple measurements and the reference probes was within ±0.05 K. After the calibration, the accuracy of the temperature differences measured using the three-junction thermopile was ±0.03 K. The values of the type B uncertainties for the directly measured quantities and the expanded uncertainties for derived quantities are reported in Table 1. For additional details on the instruments, the data reduction technique and the uncertainty analysis, the reader can refer to [23,28].

3. Experimental results

In this Section, the results obtained during condensation of steam on the MTO-450 and MTO-300 coated surfaces are presented. These new data are also compared to measurements previously obtained for a PM-200 sol–gel coated surface, which are taken from Tancon et al. [27]. The procedure for the fabrication of the PM-200 coating and its complete characterization are described in Parin et al. [29].

3.1. Characterization of the engineered surfaces

The mirror polished substrate exhibited an advancing contact angle $\theta_a = 60°$ and a receding contact angle $\theta_r < 10°$. After coating deposition, the wettability of the functionalized surfaces changed significantly, resulting in a marked reduction of the contact angle hysteresis compared to the untreated aluminum ($\Delta\theta \approx 60°$). The MTO-450 coated surface was characterized by an advancing contact angle $\theta_a = 54° \pm 3°$ and a receding angle $\theta_r = 30° \pm 3°$, while the MTO-300 coated surface exhibited slightly lower wettability, with an advancing contact angle $\theta_a = 71° \pm 3°$ and a receding contact angle $\theta_r = 49° \pm 4°$. Thus, both developed surfaces were hydrophilic with reduced contact angle hysteresis compared to the baseline aluminium. Despite the similar contact angle hysteresis ($\Delta\theta \approx 25°$), the MTO-450 sample exhibits lower contact angles than the MTO-300 sample, indicating a more hydrophilic behaviour. To finalize the characterization of the samples, FTIR measurements were conducted. The results indicated the simultaneous presence of –CH3, octyl and methyl groups, which contribute to increased contact angles, compared to pure silica. Moreover, optical images confirmed homogeneous film deposition on the substrate, while ellipsometry measurements indicated a coating thickness of approximately 300 nm for both MTO films.

The data obtained using the two developed samples (MTO-450 and MTO-300) are also compared with the measurements previously obtained on a surface functionalized by another sol–gel coating (named PM-200) with lower surface wettability ($\theta_a = 87°$, $\theta_r = 64°$) compared to the MTO coated surfaces. The PM-200 coating was chosen as a reference

Table 2
Advancing and receding contact angles, contact angle hysteresis and coating thickness. The uncertainty in the contact angle measurements corresponds to the standard deviation evaluated from eight independent measurements.

Sample	θ_a [°]	θ_r [°]	$\Delta\theta$ [°]	δ_p [nm]
MTO-450	54 ± 3	30 ± 3	24 ± 3	280 ± 15
MTO-300	71 ± 3	49 ± 4	22 ± 4	300 ± 10
PM-200 [27]	87 ± 3	64 ± 2	23 ± 3	400 ± 20

among the sol–gel coatings developed for DWC promotion because of its robustness in harsh environment (high heat flux, steam in saturated conditions, and high flow velocity) [25,29]. The detailed characterization of the PM-200 coating can be found in Parin et al. [29]. Table 2 provides a summary of the dynamic contact angle and thickness measurements.

Since the interaction with water at high temperature can lead to the degradation of the silica-based sol–gel film [29], wettability and coating thickness measurements were also performed at the end of the condensation tests. After condensation, the thickness of both MTO coatings decreased moderately by about 50 nm. Furthermore, slight variations in the contact angles were observed: $\theta_a = 59^\circ \pm 3^\circ$ and $\theta_r = 29^\circ \pm 3^\circ$ on the MTO-450 sample, while $\theta_a = 69^\circ \pm 4^\circ$ and $\theta_r = 41^\circ \pm 3^\circ$ on the MTO-300 sample. The variations of contact angles (although limited) measured on the hybrid silica sol–gel coatings are primarily related to the combined effects of mechanical and chemical interaction with water, as discussed in Basso et al. [2]. Whatever the cause, these small variations in coating characteristics are not expected to affect the heat transfer and droplet population measurements, as demonstrated in the following section.

3.2. Description of the condensation modes

The condensation tests on the MTO coated surfaces were run at constant saturation temperature (T_{sat} = 107 °C) by varying the inlet temperature of the cooling water from 95 °C to 20 °C. This was done to control the surface temperature and, thus, the wall subcooling ΔT_{sub} (Eq. (3)). Fig. 2 shows the evolution in time of the inlet coolant temperature and the corresponding average wall subcooling during the tests for measuring the condensation heat flux on the MTO-450 sample. The test run was performed by sending the coolant to the test section proceeding from the highest to lowest temperature and then vice versa. The overall duration of the operations was about 5 h and a half. When reducing the inlet coolant temperature from 95 °C to 20 °C, the saturation-to-wall temperature difference increased from 0.8 K to 39 K. Then, increasing the coolant temperature back to 90 °C caused the degree of subcooling to reduce to 1.2 K.

As highlighted by the videos recorded using the high-speed camera, different condensation modes correspond to different degrees of subcooling (Fig. 3). Pure DWC with almost circular-shaped drops (white dots in Fig. 2) was observed at low values of subcooling ($\Delta T_{sub} < 2$ K), whereas FWC (black dots in Fig. 2) covered the entire surface at high subcooling ($\Delta T_{sub} > 25$ K). Intermediate ΔT_{sub} conditions resulted in the progressive transition from DWC to FWC with an increasing presence of rivulets and flooded zones as heat flux increased (light grey and grey dots in Fig. 2). In the region of intermediate subcooling, two further condensation modes can be distinguished. For subcooling degrees below 6 K, DWC is characterized by elongated drops and rivulets. In contrast, for higher values of subcooling, progressive flooding of the surface starting from the bottom part of the surface was observed. The transition from DWC to FWC appears to occur when the condensation rate exceeds the one obtained from droplet removal by coalescence and sweeping.

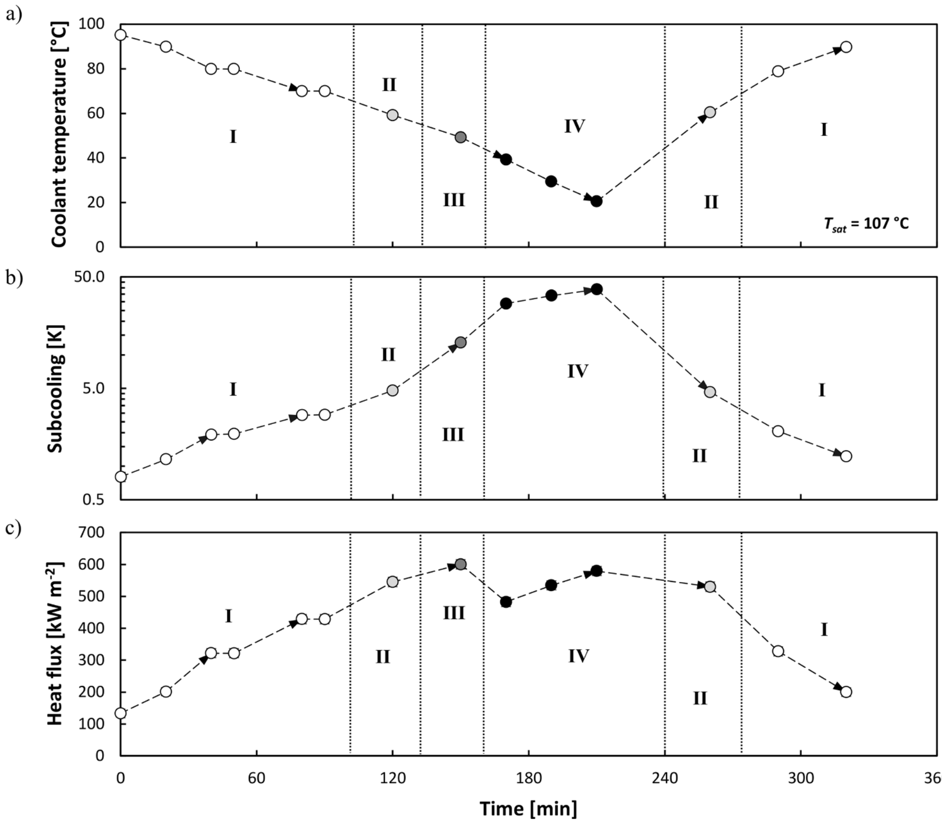

Fig. 2. Steam condensation tests on the MTO-450 sample at constant T_{sat} = 107 °C. a) Coolant inlet temperature; b) surface subcooling; c) heat flux vs time. The different condensation regimes are indicated: I) pure DWC (white dots), II) DWC with rivulets (light grey dots), III) transition DWC/FWC (grey dots), IV) FWC (black dots).

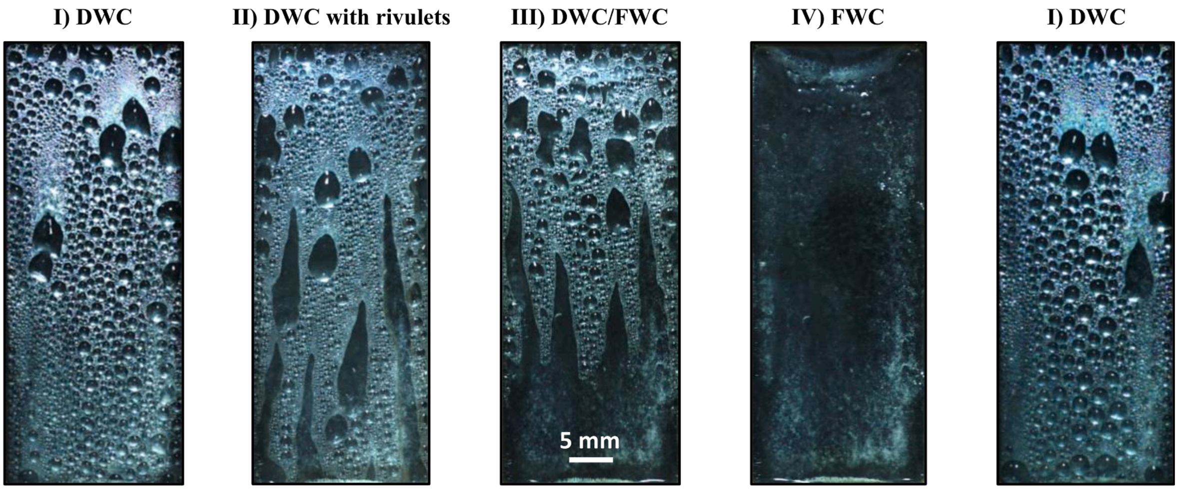

I) DWC	II) DWC with rivulets	III) DWC/FWC	IV) FWC	I) DWC
Time = 20 min	Time = 80 min	Time = 150 min	Time = 210 min	Time = 320 min
ΔT_{sub} = 1.2 K	ΔT_{sub} = 2.9 K	ΔT_{sub} = 11.5 K	ΔT_{sub} = 39 K	ΔT_{sub} = 1.3 K
q = 201 kW m^{-2}	q = 429 kW m^{-2}	q = 600 kW m^{-2}	q = 580 kW m^{-2}	q = 198 kW m^{-2}

Fig. 3. Images taken during condensation on the MTO-450 coated surface when varying the coolant inlet temperature (between 90 °C and 20 °C) and thus the wall subcooling ΔT_{sub}. The corresponding condensation regime, time, wall subcooling and heat flux are reported.

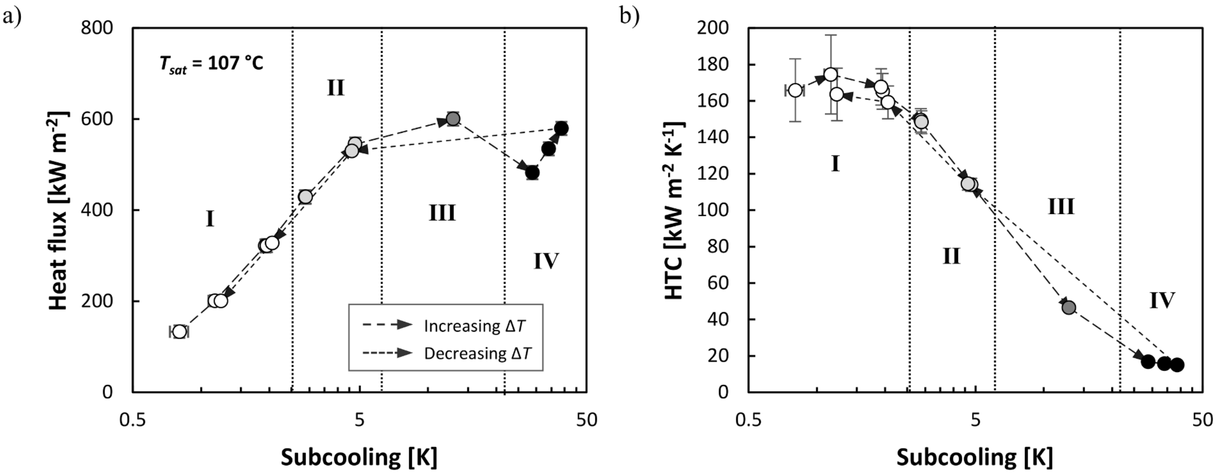

Fig. 4. Steam condensation on the MTO-450 sample at constant T_{sat}. a) Heat flux and b) HTC vs surface subcooling. The different condensation regimes are indicated: I) pure DWC (white dots), II) DWC with rivulets (light grey dots), III) transition DWC/FWC (grey dots), IV) FWC (black dots). Connecting arrows indicate the sequence of the test run.

Once flooding of the surface was achieved at the highest wall subcooling, reversion to pure DWC was observed when increasing the coolant temperature and thus reducing wall subcooling and the heat flux.

In Fig. 4a and 4b, the average heat flux and HTC measured during condensation of steam on the MTO-450 sample are plotted against surface subcooling. The obtained condensation curve can be divided into four regions. In the first region (I), for $\Delta T_{sub} < 2$ K, the heat flux increases almost linearly with subcooling, resulting in constant HTC values of about 170 kW m^{-2} K^{-1}. Region I corresponds to pure DWC condensation mode. In the second region (II), for values of ΔT_{sub} between 2 K and 6 K, the heat flux increases sublinearly with subcooling. This results in a decrease of the HTC, which, however, remains considerably higher (>100 kW m^{-2} K^{-1}) compared to traditional FWC. As shown in Fig. 3, the condensation mode in region II can be classified as DWC with elongate drops and rivulets.

Further increasing the subcooling results in the transition from DWC to FWC, with progressive flooding of the condensing surface starting from the bottom. Within the DWC/FWC transition region (III), for values of ΔT_{sub} from 6 K to 12 K, the heat flux continues to increase until it reaches a maximum value of about 600 kW m^{-2}, corresponding to a flooded area of the condensing surface of about 25 %. Further increasing the subcooling up to $\Delta T_{sub} \approx 12$ K causes the heat flux to decrease. The local minimum value of heat flux ($q \approx 450$ kW m^{-2}) is expected in correspondence to the complete flooding of the surface ($\Delta T_{sub} \approx 25$ K). In region III, the HTC strongly decreases approaching the values of FWC. In the last region of the condensation curve (IV), for $\Delta T_{sub} > 25$ K, the condensation mode corresponds to FWC: the heat flux increases again with subcooling, while the HTC decreases. For the lowest cooling water temperature (20 °C), the surface subcooling and heat flux were respectively equal to 39 K and 580 kW m^{-2}, corresponding to an HTC value of 15 kW m^{-2} K^{-1}.

When increasing the cooling water temperature from 20 °C to 60 °C, reversion from FWC to DWC with rivulets condensation was observed. Thus, the subcooling was strongly reduced from about 40 K to 4.6 K with a slightly reduction of the heat flux from 580 to 530 kW m^{-2}. Consequently, the HTC rose from 15 to 114 kW m^{-2} K^{-1}. Further increase in the coolant temperature up to 90 °C led to the recovery of pure DWC with HTC values close to those measured at the beginning of the test run

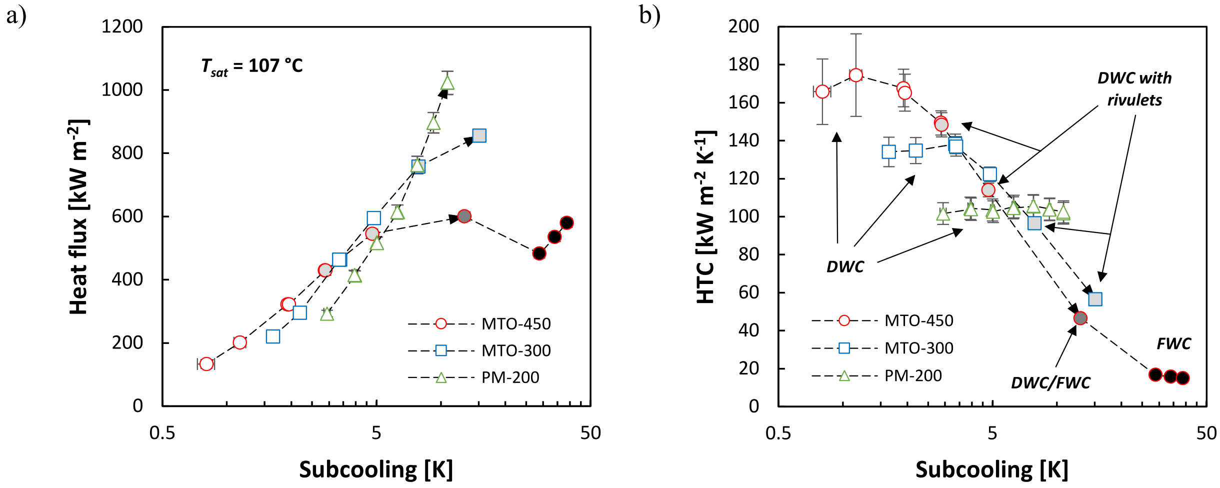

Fig. 5. Heat transfer measurements during steam condensation on the two fabricated surfaces (MTO-450 and MTO-300) at constant T_{sat}. a) Heat flux and b) HTC vs wall subcooling. Data obtained on the PM-200 sample by Tancon et al. [27] are also reported for comparison.

(Fig. 4b). It is worth mentioning that the MTO-450 coating was tested on two different samples, yielding results in excellent agreement.

With regard to the condensation curve presented in Fig. 4, one question remains unanswered: what is the mechanism governing the DWC/FWC transition? As discussed in the Introduction, there are two main theories to explain the transition [13]. The first theory assumes that, for sufficiently high wall subcooling, the rate at which new portions of the surface are cleaned by coalescence and sweeping events is not sufficient to sustain the increasing condensation rate. This results in the flooding of the surface, starting from downstream. The second hypothesis is that increasing the saturation-to-wall temperature difference activates smaller nucleation sites, which may potentially result in the formation of a continuous film. This question will be addressed in the following section.

3.3. Effect of wettability on DWC/FWC transition

The condensation curve vs subcooling measured for the MTO-300 sample is presented in Fig. 5, alongside that obtained for the MTO-450 surface, which has already been presented in Fig. 4. In particular, the average heat flux and HTC measured during steam condensation on the MTO-450 sample are respectively plotted against surface subcooling in Figs. 5a and 5b. For comparison, the heat transfer measurements obtained on a sol–gel surface with lower wettability (named PM-200) taken from a previous work [27] are also reported. These data refer to inlet cooling water temperatures ranging from 80 °C to 5 °C, saturation temperature of about 106 °C, and average inlet vapor velocity of 5.5 m s^{-1}. In Table 2, the values of contact angles and thickness for the PM-200 coating are summarized. For detailed characterization of the coating, the reader is referred to Parin et al. [29]. Before condensation, the thickness of the PM-200 coating was approximately 400 nm, while the advancing and receding contact angles were respectively equal to 87° and 64°. After condensation, the coating thickness remained almost the same, while the contact angles underwent to minor variations ($\theta_a = 82^\circ$ and $\theta_r = 60^\circ$).

These three surfaces allow for the investigation of the effect of surface wettability on the condensation curve. It is notable that, despite the similar contact angle hysteresis ($22^\circ < \Delta\theta < 24^\circ$), the MTO-450 displays greater hydrophilicity, with an equilibrium contact angle of 43° ($\theta_e = \cos^{-1}(0.5\cos(\theta_a) + 0.5\cos(\theta_r))$, whereas the PM-200 sample exhibits the

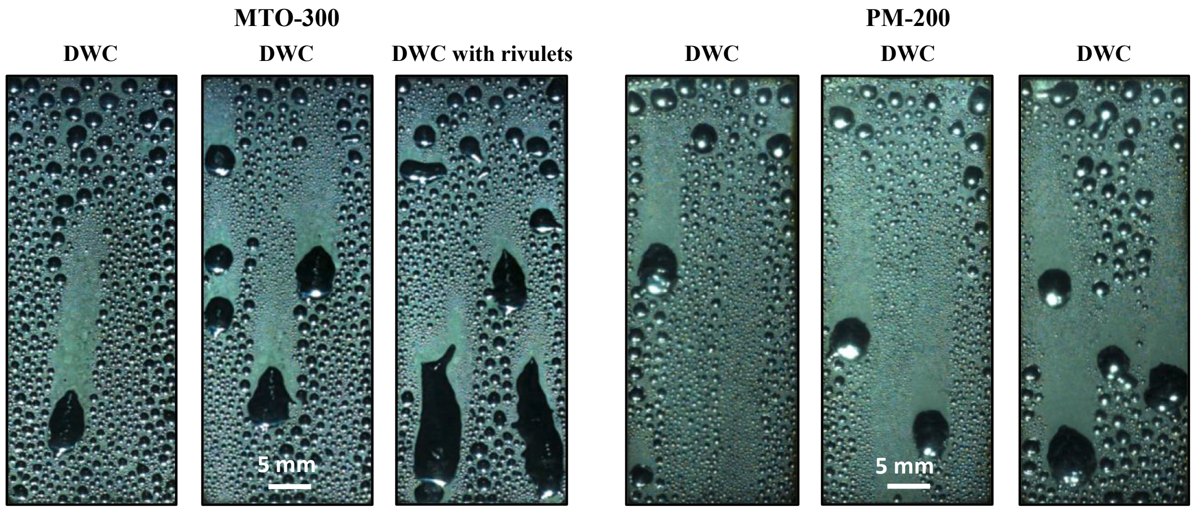

ΔT_{sub} = 2.2 K
q = 295 kW m^{-2}

ΔT_{sub} = 4.9 K
q = 594 kW m^{-2}

ΔT_{sub} = 15. 2 K
q = 855 kW m^{-2}

ΔT_{sub} = 2.9 K
q = 293 kW m^{-2}

ΔT_{sub} = 6.3 K
q = 613 kW m^{-2}

ΔT_{sub} = 8.8 K
q = 896 kW m^{-2}

Fig. 6. Images of condensation recorded on the MTO-300 and PM-200 coated surfaces for different cooling water inlet temperatures: 80 °C, 50 °C and 20 °C. The corresponding wall subcooling and heat flux are reported.

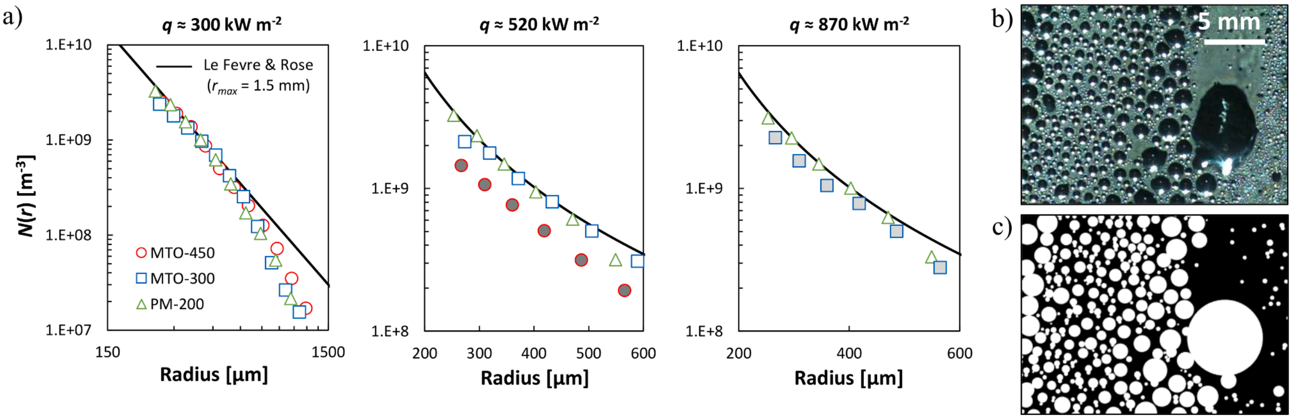

Fig. 7. a) Measurements of drop-size density $N(r)$ vs drop radius on the three samples. The data refers to three values of heat flux (obtained with coolant temperatures of 80 °C, 50 °C, and 20 °C). The Le Fevre and Rose [36] correlation obtained with $r_{max} = 1.5$ mm is also reported. Empty symbols refer to pure DWC, light grey symbols to DWC with rivulets, grey symbols to transition DWC/FWC. b) Image of DWC and c) resulting reconstructed image (in black and white).

least hydrophilic behaviour, with an equilibrium contact angle of 76°. The MTO-300 sample exhibited an intermediate behaviour with $\theta_e = 61^\circ$.

For low values of subcooling, the condensation curves for the MTO-300 and PM-200 samples exhibit a similar trend compared to that obtained for the MTO-450 sample, which instead covers all the different condensation modes from DWC to FWC. In particular, with respect to the four different regions of the condensation curve shown in Fig. 4, the measurements performed on the MTO-300 sample only cover the first two regions (I and II), characterized by DWC and DWC with rivulets condensation modes, while those on the PM-200 surface correspond to the first region (I), characterized by pure DWC mode. In fact, for the MTO-300 sample, the heat flux increases almost linearly with subcooling up to $\Delta T_{sub} \approx 5$ K, resulting in constant HTC values of about 130 kW m^{-2} K^{-1}; the condensation mode is pure DWC (Fig. 6). When the subcooling exceeds 5 K, the heat flux increases sublinearly with subcooling, resulting in a decrease of the HTC. The minimum coolant temperature of 20 °C corresponds to a subcooling of 15 K and a heat flux of 855 kW m^{-2} (HTC ≈ 56 kW m^{-2} K^{-1}). As shown in Fig. 6, in this range of subcoolings, the condensation mode gradually changes from pure DWC with almost circular drops to DWC with elongated drops and rivulets, particularly at the bottom of the surface.

On the other hand, the less hydrophilic PM-200 sample only presents the region of the condensation curve where the heat flux linearly increases in the entire range of subcooling ($3\text{ K} < \Delta T_{sub} < 11$ K), reaching a maximum value of 1020 kW m^{-2} for $\Delta T_{sub} = 11$ K. The images recorded during condensation revealed that the condensation mode on the PM-200 surface was pure DWC in the entire subcooling range (Fig. 6).

The results clearly show that the peak of the heat flux curve, as well as the transition from DWC to FWC, was not achieved for either the MTO-300 and PM-200 samples, which have both higher contact angles ($\theta_e = 61^\circ$ and $\theta_e = 76^\circ$, respectively) compared to the more hydrophilic MTO-450 sample ($\theta_e = 43^\circ$). However, in the case of the MTO-300 sample, which is more hydrophilic than the PM-200 sample, it is possible to observe a flexion of the condensation curve corresponding to the transition from pure DWC to DWC with rivulets, which is characterized by lower HTCs compared to pure DWC. Further increase in surface subcooling is expected to cause the flooding of the bottom area of the condensing surface, as observed for the MTO-450 coated sample (Fig. 3).

As shown in Fig. 5, the higher the surface wettability, the higher the HTC that can be achieved during DWC due to the enhanced nucleation and lower conduction thermal resistance of the droplets [10,30]. In particular, the HTC values measured on the MTO-450 sample ($\theta_e = 43^\circ$) are 30 % higher than those obtained on the MTO-300 sample ($\theta_e = 61^\circ$) and 70 % higher compared to the PM-200 sample ($\theta_e = 76^\circ$). It is important to note that the lower HTC values measured for the PM-200 sample may be partially attributed to the higher thermal resistance of the coating. Since the HTC calculated using Eq. (1) accounts also for the coating thermal resistance, it can be deduced that the greater thickness of the PM-200 film (~400 nm) compared to the two MTO coatings (~290 nm), combined with the typical thermal conductivity of sol–gel silica-based coatings (in the range 0.1–0.3 W m^{-1} K^{-1} [31,32]), could contribute to a reduction of the heat transfer.

Conversely, for comparable contact angle hysteresis, the more hydrophilic is the condensing surface, the lower the surface subcooling and heat flux values that can be achieved while promoting pure DWC. For the MTO-450 sample, pure DWC with constant HTC was maintained only up to a subcooling of about 2 K and a heat flux of 350 kW m^{-2}. Due to the lower wettability, the MTO-300 sample was able to sustain DWC with constant HTC values over a broader range of subcooling and heat flux ($\Delta T_{sub} < 5$ K, $q < 600$ kW m^{-2}), whereas the less hydrophilic PM-200 sample sustained pure DWC across the entire range of wall subcooling ($\Delta T_{sub} < 10$ K) and heat flux ($q < 1000$ kW m^{-2}) here investigated.

The results presented in Fig. 5 suggest that surface wettability plays a key role in determining the shape of the condensation curve vs subcooling. For a vertical oriented surface, at low vapor velocities, the droplet removal efficiency is mainly related to gravity force and droplet adhesion force (which in turn depends on the surface wettability) [24]. Specifically, for a given $\Delta\theta$, the droplet removal efficiency increases with the equilibrium contact angle, resulting in smaller droplet departing radii [33,34]. In particular, the departing radius measured on the PM-200 surface ($r_{max} = 1.3$ mm) are 40 % smaller than those measured on the MTO-450 surface ($r_{max} = 1.8$ mm). Therefore, it can be expected that the lower the surface wettability (and thus the higher the condensate removal efficiency), the higher the values of subcooling and heat flux that the surface can withstand before transiting from DWC to FWC. This results in a shift of the condensation curve peak towards the top-right edge of the q-ΔT_{sub} chart. Therefore, it seems plausible that the transition from DWC to FWC occurs when the condensation rate exceeds the one obtained from droplet removal.

For the same investigated range of coolant temperature, the transition from DWC to FWC was only observed for the more hydrophilic surface (MTO-450). The higher droplet removal efficiency of the MTO-300 and PM-200 samples allowed DWC to be sustained over a wide range of surface subcooling, resulting in higher values of heat flux that can be achieved (Fig. 5). The surface wettability could also explain the differences in the condensation mode between the MTO-300 and PM-200 sample. At high heat flux values, the rivulets are present on the MTO-300 surface, which exhibits a lower θ_e and thus a lower condensate removal efficiency. Furthermore, the role of surface wettability on DWC-

Table 3
Total area occupied by elongated droplets and/or rivulets at different operating conditions.

Sample	T_{cool} [°C]	q [kW m^{-2}]	A^* [%]
MTO-450	80	321	9
	50	600	33
MTO-300	80	295	5
	50	594	14
	20	855	25
PM-200	80	292	4
	50	613	7
	20	896	13

FWC transition could also explain the results present in the literature [13–15,20].

To further understand the dropwise condensation HTC decrease with increasing subcooling (and thus heat flux), the droplet population was investigated. First, the videos recorded by the high-speed camera were analysed using a custom MATLAB® script (which is described with more details in [35]) for the determination of the average drop-size distribution (Fig. 7). Figs. 7b and 7c show an example of the investigated area of the sample (15 mm × 21 mm) and the reconstructed image obtained by the MATLAB® program. The experimental uncertainty associated with the drop-size distribution measurement is less than 12 %. Briefly, to obtain the drop-size distribution, the whole range of measured radii is divided into multiple bins (classes). Each droplet is counted into a specific class based on its radius. These stages are repeated iteratively for each frame of the video, allowing the evaluation of the drop-size distribution. The present optical setup allowed for the accurate detection of droplet radii above 250 µm. Fig. 7a displays the drop-size distribution measured on the MTO-300, MTO-450, and PM-200 samples under three different heat flux conditions (300, 520, 870 kW m^{-2}). The experimental data are compared with the well-known model by Le Fevre and Rose [36] for the drop-size distribution of large droplets $N(r)$:

$$N(r) = \frac{1}{3\pi r^2 r_{max}} \left(\frac{r}{r_{max}}\right)^{-2/3} \tag{6}$$

where r_{max} is the droplet departing radius.

As a further step, the videos recorded under different operating conditions were analysed in order to evaluate the average area (A^*) of the surface filled by drops with a radius larger than r_{max}, elongated droplets and rivulets. Indeed, due to the high thermal conduction resistance through the increased liquid thickness of elongated droplet and rivulets, areas occupied by the large aggregation of condensate are expected to less contribute to the DWC heat transfer. Furthermore, the presence of flooded areas prevents the renewal of the surface (with the nucleation of new droplets) and consequently hinders the heat transfer. For each video, 12 frames corresponding to 1 s of condensation were analysed. In each video frame, the area occupied by sweeping drops and rivulets has been measured. Finally, all the areas detected for one sequence of frames were summed, divided by the number of frames analysed and by the area of the sample (20 × 50 mm^2) to obtain an average value. These results are reported in Table 3.

The graph corresponding to $q \approx 300$ kW m^{-2} covers the entire range of investigated radii (from 250 µm to 1400 µm). The drop-size distribution on the three samples exhibits a decreasing trend as the radius increases and comparable values of $N(r)$. This similarity in trend and values can be explained considering that, at such low heat flux, the three samples promote DWC without the formation of elongated drops or rivulets. Comparing the results with the Le Fevre and Rose [36] model considering $r_{max} = 1.5$ mm (which is the average of the values measured on the three surfaces), an average deviation of approximately 10 % was found for all samples in terms of droplet radii smaller than 600 µm. As the droplet size increases, measured values deviate from model predictions due to the sweeping effect of the falling droplets. In fact, the shape of $N(r)$ near r_{max} deviates downward compared to the power law trend formulated by Le Fevre and Rose [36] which does not account for this effect. Overall, these results indicate that major part of the surface is working in DWC mode, without significant portions (less than 10 %) of the surface occupied by obstacles to the heat transfer (Table 3).

In order to facilitate the comparison of the various samples, the experimental data obtained at higher heat flux values are focused onto a narrow range of droplet radii (200–600 µm), thus excluding the larger droplets which contribute less to the heat transfer [26]. At $q = 520$ kW m^{-2}, since the condensation mode for both the MTO-300 and PM-200 remains pure DWC, the drop-size distributions continue to follow the Le Fevre and Rose [36] equation with good agreement. On the contrary, the condensation mode on the MTO-450 coated surface has turned into DWC with rivulets. In fact, due to the presence of rivulets, the average area available for DWC decreased by 33 %, resulting in a reduction by about 50 % of the drop-size density in the considered range of droplet radii (200–600 µm). At the highest heat flux (about 870 kW m^{-2}), only the data sets for the PM-200 and MTO-300 samples are reported, as the MTO-450 sample exhibited a transition from DWC to FWC for the same temperature of the cooling water (20 °C). As a consequence of the enhanced condensation rate, the MTO-300 sample (which is more hydrophilic than the PM-200 surface) was not able to maintain pure DWC, resulting in the formation of elongated drops and some short rivulets, which reduced the surface area available for the formation and growth of drops by 25 %. Thus, the density of drops with radii between 250 and 600 µm decreased by 24 % compared to the PM-200 sample, which instead remained consistent with the Le Fevre and Rose [36] model.

4. Modeling of DWC heat transfer and DWC/FWC transition on hydrophilic surfaces

This section addresses the modelling of dropwise condensation on hydrophilic surfaces. It presents a comprehensive procedure for calculating the steady-state DWC heat flux and for predicting the maximum surface subcooling that can be applied to a surface while promoting DWC, before the transition to FWC occurs. Finally, the calculation method is validated by comparing the numerical results with the heat transfer data presented in Section 3.

4.1. Heat transfer model

The time-averaged heat flux transferred during DWC (q) obtained by combining the heat flow rate through a single drop (Q_d) with the average drop-size distribution on the condensing surface can be expressed as:

$$q = \int_{r_{min}}^{r_e} Q_d(r)\ n(r)\ \mathrm{d}r + \int_{r_e}^{r_{max}} Q_d(r)\ N(r)\ \mathrm{d}r \tag{7}$$

In Eq. (7), $n(r)$ and $N(r)$ are, respectively, the drop-size density function of small and large drops, r_e is the effective radius (i.e., the threshold radius between the two distributions), r_{min} is the radius of the smallest thermodynamically viable drop, and r_{max} is the departing radius.

The minimum droplet radius is evaluated according to the nucleation theory [37] as:

$$r_{min} = \frac{2\ \sigma\ T_{sat}}{\rho_l\ h_{lv}\ \Delta T_{sub}} \tag{8}$$

where σ is the surface tension, ρ_l is the liquid density, h_{lv} is the latent heat of vaporization.

The effective radius is evaluated assuming the nucleation sites distributed according to the Poisson distribution [38] as:

$$r_e = \frac{1}{4\ \sqrt{N_s}} \tag{9}$$

where N_s is the density of nucleation sites on the condensing surface. The literature on DWC of pure steam reports a broad range of values for the nucleation site density (10^{10}–10^{15} m^{-2}) [4]. The choice of N_s will be further discussed in Section 4.3.

In order to predict the combined effects of vapor velocity and surface inclination on the DWC heat flux, the departing radius is evaluated as suggested by the present authors in [25,39]:

$$\begin{cases} r_{max} = \dfrac{-C+\sqrt{C^2+4AB}}{2B}, & 0^\circ < \beta \leq 90^\circ \\ r_{max} = \dfrac{A}{C}, & \beta = 0^\circ \end{cases} \tag{10}$$

where the A, B and C coefficients are evaluated as follows:

$$A = 2k_c \sin(\theta_e)\sigma(\cos\theta_r - \cos\theta_a) \tag{11}$$

$$B = \frac{1}{3}\left(2 - 3\cos\theta_e + \cos^3\theta_e\right)\sin(\beta)\pi\rho_l g \tag{12}$$

$$C = \frac{1}{2}\ \rho_v\ v_v^2\ C_d(\theta_e - \sin\theta_e\cos\theta_e) \tag{13}$$

where k_c is a constant (named retention factor) that depends on the drop shape, β is the inclination of the condensing surface from the horizontal, g the gravity acceleration, C_d is the drag coefficient.

For the population of large droplets ($r_e < r < r_{max}$), the drop-size density function $N(r)$ is calculated using the Le Fevre and Rose [36] model (Eq. (6)). Whereas, for the small droplet population ($r_{min} < r < r_e$), the resolution of the population balance theory [40] leads to express the drop-size density function of small droplets $n(r)$ as:

$$n(r) = N(r_e)\frac{r(r_e - r_{min})(A_2 r + A_3)}{r_e(r - r_{min})(A_2 r_e + A_3)}\ e^{B_1 + B_2} \tag{14}$$

For the analytical expressions of parameters A_1, A_2, A_3, B_1 and B_2, the reader is referred to the original work by Miljkovic et al. [38]. It is worth noting that the drop-size distribution can also be determined through numerical simulations without relying on any statistical assumptions [41–43]. Nevertheless, in order to simulate DWC on hydrophilic surfaces, the required large departing radii ($r_{max} > 1$ mm) and high nucleation site densities (10^{10} $m^{-2} < N_s < 10^{15}$ m^{-2}) requests long computational time.

The heat exchanged by a single droplet is evaluated employing the Lethuillier et al. [44] model, which offers the widest validity range for droplet Biot number ($10^{-4} < \mathrm{Bi} < 10^5$) and dynamics contact angles (20°-170°). In particular, the flow rate through a single droplet can be expressed as:

$$Q_d = \frac{\pi r^2\left(1 - \frac{r_{min}}{r}\right)\Delta T}{\frac{\delta_{HC}}{\lambda_{HC}\sin^2\theta_e} + \frac{1}{2h_i(1-\cos\theta_e)} + \frac{\pi r}{\lambda_l} f(\theta_e, \mathrm{Bi})} \tag{15}$$

where h_i is the interfacial heat transfer coefficient calculated as described in Miljkovic et al. [38], λ_p and δ_p are respectively the thermal conductivity and thickness of the promoter film, and the factor $f(\theta_e, \mathrm{Bi})$ is calculated as follows:

$$\begin{cases} f(\theta_e,\mathrm{Bi}) = \zeta_0[\tanh(\zeta_1 - \log\mathrm{Bi}) - \tanh(\zeta_2 + \zeta_3\log\mathrm{Bi}) + \zeta_4], & 10^{-2} < \mathrm{Bi} < 10^5 \\ f(\theta_e,\mathrm{Bi}) = \zeta_0\zeta_4, & \mathrm{Bi} < 10^{-2} \end{cases} \tag{16}$$

$$\zeta_i = \sum_{j=0}^{6} a_{i,j}\ \theta_e^j\ + b_i \tan\frac{\theta_e}{2} \tag{17}$$

The analytical expressions of $a_{i,j}$ and b_i can be found in the original manuscript by Lethuillier et al. [44].

Since the condensation heat flux (which is the primary result of the heat transfer model) is necessary for calculating the average vapor velocity along the condensing surface, which in turn is used to determine the departing radius by Eq. (10), an iterative procedure is required. From an initial trial value for r_{max}, the drop-size density functions and single-droplet heat transfer model are solved to obtain an initial value for the DWC heat flux q (Eq. (7)). At the next iteration, the heat flux from the former iteration is used to calculate the outlet vapor velocity and, thus, the average vapor velocity along the sample length. Then, the remaining equations are solved, resulting in an updated value for the DWC heat flux. The iterative procedure stops when the variation of q between two consecutive iterations is below 10^{-3} W m^{-2}.

4.2. Model for condensation mode prediction

The aim of this section is to present a simplified model that can be employed to predict the condensation mode (DWC or FWC/transition) on a functionalized surface. In particular, it can be used to determine the maximum values of subcooling and heat flux that a surface can withstand before the transition from DWC to FWC, in accordance with specific operating conditions and wettability.

The authors hypothesize that, in the case of DWC-FWC transition governed by surface condensate removal efficiency (as evidenced by the experimental data presented in Section 3), stable DWC can be achieved as long as the characteristic time required for droplet removal (τ_{sweep}) is smaller compared to the characteristic time for the droplet to grow from r_{min} to r_{max} (τ_{growth}), i.e. as long as the sweeping process can be considered "fast" compared to the droplet growth process. On the other hand, the transition from DWC to FWC, and eventually the complete flooding of the condensing surface, is expected to occur when the growth time becomes shorter than the removal time ($\tau_{growth} < \tau_{sweep}$). This criterion is summarized as:

$$\begin{cases} \text{DWC} & if \quad \tau_{growth} > \tau_{sweep} \\ \text{Transition/FWC} & if \quad \tau_{growth} < \tau_{sweep} \end{cases} \tag{18}$$

It is expected that the time required for droplet removal by sliding is likely to remain constant when the surface wettability, the length of the condensing surface along the sliding direction, and the vapor velocity are kept constant. On the other hand, the time required for droplet growth is expected to decrease significantly with increasing subcooling (and thus with increasing heat flux). For the sake of simplicity, the formation of rivulets during the transition from pure DWC to FWC is not considered. This decision aligns with the primary objective of the developed model, which is to identify the range of wall subcooling over which the DWC heat transfer model described in Section 4.1 can be applied. To account for the effect of rivulets on condensation heat transfer, dedicated models can be implemented [45,46].

As described in Eq. (19), the characteristic droplet growth time is calculated as the sum of the time required for a droplet to grow by direct condensation of vapor from r_{min} to r_e (τ_{cond}) and the time required for the droplet to grow by coalescence from r_e to r_{max} (τ_{coal}).

$$\tau_{growth} = \ \tau_{cond} + \tau_{coal} \tag{19}$$

Under the assumption that all the heat transfer during DWC occurs through the drops, the heat transfer rate of a single drop (Eq. (15)) can be equated to the latent heat of phase change at the droplet surface ($Q_d = \rho_l\, h_{lv}\, dV/d\tau$) to obtain the infinitesimal time $d\tau_{growth}$ required for a droplet to grow by an infinitesimal radius dr:

$$d\tau_{cond} = \ \rho_l\, h_{lv}\, \pi\ \left(2 - 3\cos\theta_e + \cos^3\theta_e\right) Q_d^{-1}(r)\, r^2 dr \tag{20}$$

The integration of Eq. (20) between r_{min} and r_e yields τ_{cond}.

As described in Yamali and Merte [47], the time period τ_{coal} required for the droplet to grow by coalescence from r_e to r_{max} can be calculated by integrating the following differential equation:

Table 4
List of input parameters used for the prediction of dropwise condensation HTCs and condensation mode.

Parameter		MTO-450	MTO-300	PM-200
ΔT	[K]	0.8–2	1.6–4.9	2.9–10.7
T_{sat}	[°C]	107	107	107
v_v	[m s^{-1}]	3.5	3.5	5.5
θ_a	[°]	54	71	87
θ_r	[°]	30	49	64
λ_p	[W m^{-1} K^{-1}]	0.2	0.2	0.2
δ_p	[nm]	280	300	400
N_s	[m^{-2}]	2 × 10^{12}	2 × 10^{12}	2 × 10^{12}
$\Delta\tau$	[ms]	1	1	1
L	[m]	0.05	0.05	0.05

$$d\tau_{coal} = \frac{\frac{n\,\rho_l\,h_{lv}\left(2-3\cos\theta_e+\cos^3\theta_e\right)}{3\,(n+1)}\left(1+n\,r_e^{n+1}\,r^{-\,(n+1)}\right)}{q}\,dr \tag{21}$$

Where $n = 1/3$ is the exponent of the function obtained by Le Fevre and Rose [36] for the distribution of large drops.

The characteristic time for droplet sliding is here calculated by implementing a model describing the droplet motion on a solid surface. Solving the balance of forces acting on the moving drop, the droplet velocity (u_d) can be obtained from the following differential equation:

$$\rho_l\,V(r)\,\frac{du_d}{dt} = F_g(r) + F_{drag}(r) - F_{ad}(r) - F_f(u_d, r) \tag{22}$$

where V is the droplet volume, F_{ad} is the adhesion force evaluated as $F_{ad} = A\,r$, F_g is the gravity force calculated as $F_g = B\,r^3$, F_{drag} is the drag force acting on the drop obtained as $F_{drag} = C\,r^2$, F_f is the viscous force acting on the droplet accounting for both the bulk and wedge (i.e., contact line) contributions, calculated according to Wang and Zhao [48]. The parameters A, B and C are calculated by Eqs. (11)–(13). By determining the velocity function in the variable of time, it is possible to calculate the time τ_{sweep} required for the droplet to move from its initial position at the top of the surface ($x = 0$) to the lower edge ($x = L$). For the sake of simplicity, it is assumed that the droplet moves in a straight line and maintains a circular contour during the sliding process.

When considering a droplet moving with a variable volume, such as on a condensing surface where drops grow along their sliding due to coalescence, the solution of the differential equation (Eq. (22)) requires the knowledge of the droplet growth function throughout its motion. Assuming an average drop-size distribution on the condensing surface calculated according to Le Fevre and Rose [36], the droplet growth function during the sliding process can be evaluated as follows:

$$dr = \frac{2\,r\,u_d\left[\int_{r_e}^{r_{max}} N(r)\,\frac{\pi}{3}\left(2-3\cos\theta_e+\cos^3\theta_e\right)r^3\,dr\right]}{\pi r^2\left(2-3\cos\theta_e+\cos^3\theta_e\right)}\,d\tau \tag{23}$$

where the term within the square brackets represents the average volume of drops present on the condensing surface, according to the considered drop-size distribution. In Eq. (22), it is assumed that the width of the swept area is equal to the drop diameter.

In the present work, the droplet sliding is solved using the following numerical procedure. Initial values of droplet dimension ($r = r_{max}$) and velocity ($u_d = 0$) are assumed at the onset of the sliding process ($\tau = 0$) in order to numerically solve Eq. (22) and obtain the finite but small variation of droplet velocity (Δu_d) within the considered time step $\Delta\tau$. Consequently, the velocity of the droplet after covering a small discrete distance (Δx) can be determined. Assuming that the swept area within the time step can be calculated as $2\,r\,\Delta x$, the increment of droplet radius (Δr) due to coalescence with other droplets within the considered time step can be calculated using Eq. (23). At the next time step, the values of droplet radius and sliding velocity from the previous time step are employed as inputs to the force balance equation (Eq. (22)) for evaluating the variation of drop velocity and the discrete covered distance Δx within the new time step. Then, Eq. (23) is used to evaluate the additional increase of drop radius due to coalescence within the time step. This procedure continues until the distance covered by the sliding droplet ($\sum \Delta x$) exceeds the length of the condensing surface (L).

4.3. Comparison against experimental data

The model is here compared with the experimental data presented in Section 3. Table 4 lists all the input parameters required for the calculation of the DWC heat flux and condensation mode. For each considered surface wettability, the table provides information on the quantities (ΔT, T_{sat}, v_v), the contact angles (θ_a and θ_r), the coating thickness (δ_p) and thermal conductivity (λ_p), the nucleation sites density (N_s), time step ($\Delta\tau$), and length of the condensing surface (L). Since direct measurements of nucleation site density are challenging, the value of N_s is typically assumed. Here, a nucleation sites density of 2×10^{12} m^{-2} was chosen to best match the measured HTCs for the PM-200 surface, as previously discussed in [25]. This value is aligned with measurements reported in the literature [49,50]. In accordance with Chrobak et al. [32], the thermal conductivity of the sol–gel silica-based coating was

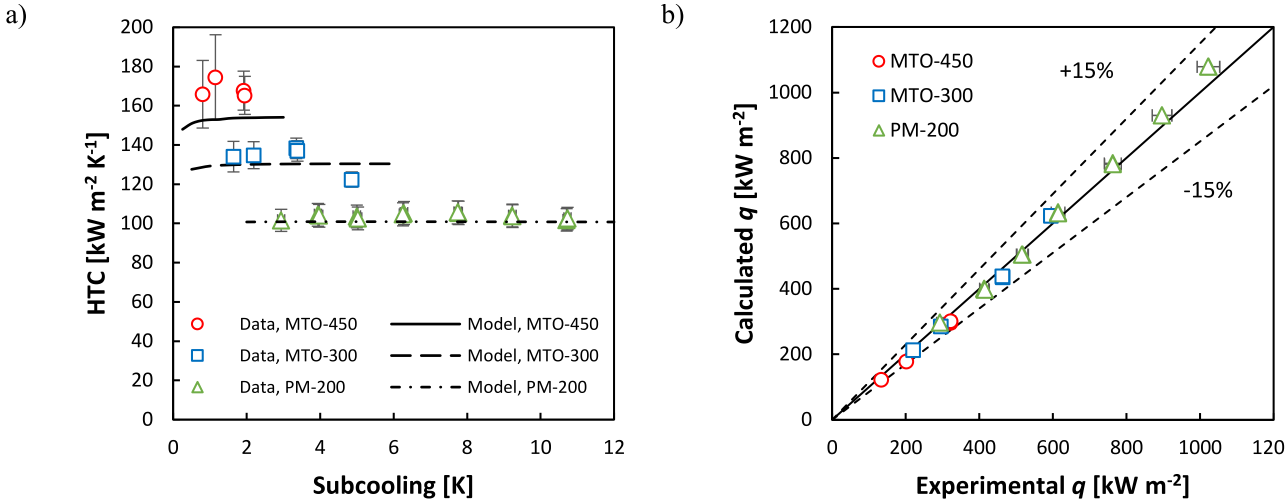

Fig. 8. Comparison between heat transfer measurements obtained during pure DWC of steam on the three surfaces with different wettability (MTO-450, MTO-300, PM-200) and predictions by the proposed calculation method (Section 4.1). a) Experimental (symbols) and calculated (lines) HTC values versus degree of subcooling. b) Experimental versus predicted heat flux q. Model inputs are listed in Table 4.

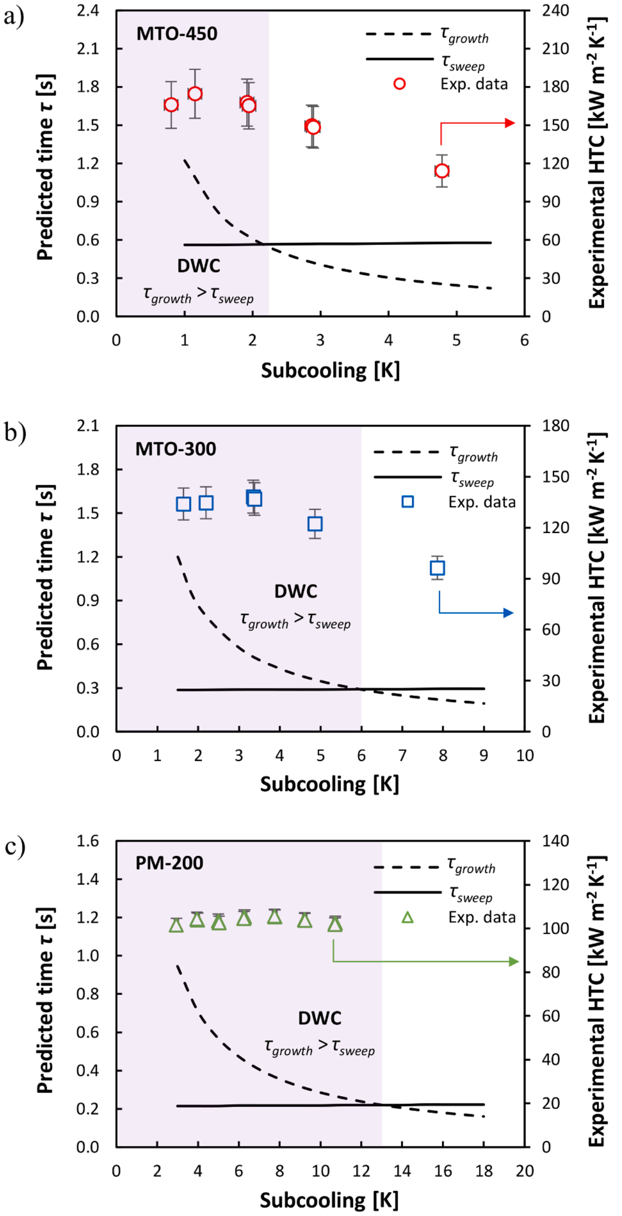

Fig. 9. Calculated characteristic times for droplet growth (τ_{growth}) and sweeping (τ_{sweep}) by the proposed model (Section 4.2) at varying surface subcooling on the three considered surfaces: a) MTO-450, b) MTO-300 and c) PM-200. The model predicts the DWC condensation mode with constant values of HTC for $\tau_{growth} > \tau_{growth}$ (purple area). The experimental values of HTC presented in Section 3 are also reported. Model inputs are listed in Table 4.

assumed to be 0.2 W m^{-1} K^{-1}.

Fig. 8 shows the comparison between experimental data and model predictions. In Fig. 8a, the measured and calculated HTCs are plotted as a function of surface subcooling. In this graph, the red, blue, and green data series represent respectively the experimental HTCs for the MTO-450, MTO-300, and PM-200 samples, while the black lines correspond to the predicted values. It can be noted that the proposed model accurately predicts the trends of HTC with surface subcooling for all the considered wettabilities. In particular, an excellent agreement between the experimental data and the model predictions is observed, with a mean relative deviation below 10 % for all three samples. Specifically, the lowest mean deviation, 3 %, was obtained for the PM-200 sample, whereas the highest deviation (12 %) was observed for the MTO-450 sample. This discrepancy can be attributed to the model's assumption of perfectly circular droplets. Indeed, for MTO-450, the high hydrophilicity leads to droplet elongation during sliding, deviating from the circular assumption. In contrast, the PM-200 sample exhibits behavior closer to that of a hydrophobic surface, characterized by nearly circular sliding droplets. Furthermore, on surface characterized by higher wettability (as the MTO-450), the nucleation sites density could theoretically be higher [30]. However, for the sake of simplicity, it has been decided to assume a unique value of N_s for all three surfaces.

Fig. 8b further corroborates the accuracy of the proposed model. This figure plots the calculated DWC heat flux by Eq. (7) against the experimental heat flux. The proposed methodology demonstrates reliable predictions of condensation heat flux, with an average relative deviation of about 6 %. Based on the observations above, it can be concluded that the presented calculation method effectively predicts the effect of surface wettability and wall subcooling on heat transfer performance during dropwise condensation.

In addition to the prediction of the DWC heat transfer, the model presented in Sections 4.1–4.2 can be used to estimate the range of surface subcooling over which DWC can be probably sustained. The results of the analysis are reported in Fig. 9, where the trends of the characteristic time for droplet growth τ_{growth} (black dashed line) and removal τ_{sweep} (black solid line) predicted by the model are plotted vs surface subcooling for each considered wettability. In addition to the characteristic times, the measurements of HTC are reported. According to the developed model (Section 4.2), it can be expected to promote and sustain DWC when $\tau_{growth} > \tau_{sweep}$, whereas transition to filmwise condensation or even flooding of the condensing surface is expected to occur when $\tau_{growth} < \tau_{sweep}$. The subcooling range corresponding to the DWC region is highlighted in purple.

In the case of the MTO-450 sample (Fig. 9a), the model predicts τ_{growth} values decreasing from 1.2 s to approximately 0.3 s as subcooling increases from 1 K to 5.5 K. This obviously is reflected in increasing condensation rates (and heat fluxes) with subcooling. On the other hand, τ_{sweep} (which mainly depends on surface wettability) remains nearly constant at around 0.6 s. The intersection of the two curves, indicating the threshold between DWC and FWC, occurs at ΔT_{sub} of about 2 K. This result is in good agreement with the experimental data, which show constant HTCs of approximately 170 kW m^{-2} K^{-1} for subcooling below 2 K and a rapid decrease in HTC beyond this threshold. Fig. 9b shows the results obtained for the MTO-300 sample. Considering the lower wettability of this surface, τ_{sweep} is lower (0.3 s) compared to MTO-450 (0.6 s). With regards to the growth time, the model predicts a decrease in τ_{growth} from 1.2 s to 0.2 s as the subcooling increases from approximately 1 K to 9 K. The condition $\tau_{sweep} = \tau_{growth}$, which corresponds to the maximum subcooling value for sustaining pure DWC, is achieved at $\Delta T_{sub} = 6$ K, demonstrating good agreement with the experimental data. Fig. 9c illustrates the model predictions for the PM-200 sample, which exhibited constant HTC values in the entire range of wall subcooling here investigated (3–11 K). Specifically, the predicted τ_{growth} decreases from 1 s to 0.15 s as subcooling increases from 2.5 K to 18 K, while τ_{sweep} remains nearly constant at around 0.2 s. The intersection between the two characteristic times occurs at a subcooling value of approximately 13 K, substantially higher compared to the maximum value experimentally tested. Therefore, pure DWC is correctly predicted for PM-200 over the entire range of subcooling.

It must be noted that the nucleation sites density must be assumed as input parameter in the model (Sections 4.1–4.2). N_s plays a crucial role in shaping the drop-size distribution and thus in determining the condensation heat flux (Eq. (7)). Since the characteristics time for droplet growth depends on q, the maximum surface subcooling for sustaining DWC is also affected by N_s. For the results reported in Figs. 8-9, a fixed value of 2×10^{12} m^{-2} was chosen for all three surfaces. However, given that N_s is difficult to infer experimentally and can vary over several orders of magnitude, a sensitive analysis was conducted to study the effect of N_s on the predictions of the developed model. According to the literature regarding DWC with pure water vapor [49,51,52], values of N_s in the range 10^{10}-10^{14} m^{-2} were assumed for

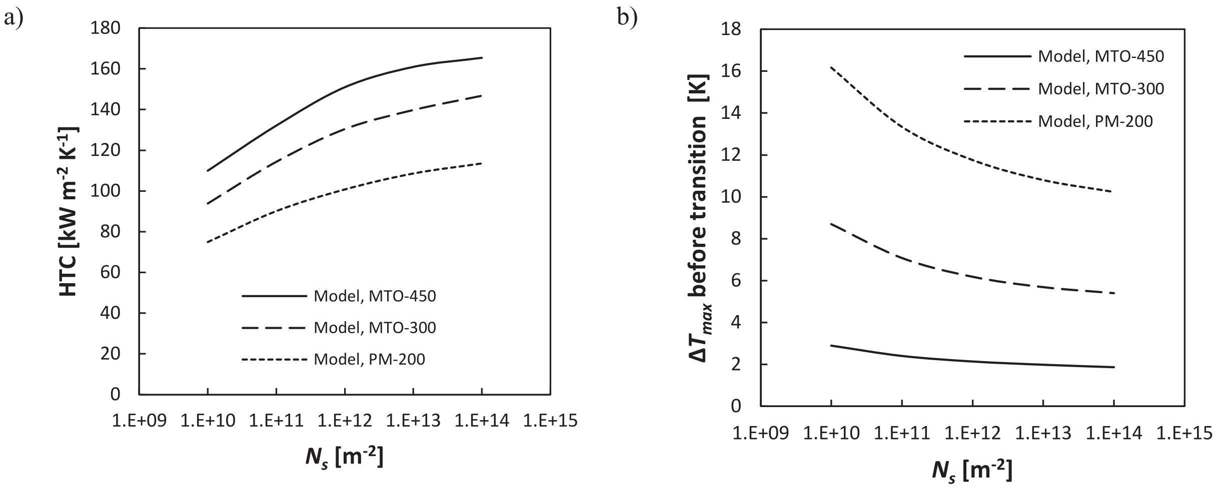

Fig. 10. Effect of nucleation sites density N_s on the predictions of the model presented in Sections 4.1-4.2. a) Predicted HTC and b) maximum surface subcooling before transition (ΔT_{max}) versus N_s for the three considered surfaces (MTO-450, MTO-300, and PM-200). The other model inputs are listed in Table 4.

the three different surfaces (MTO-450, MTO-300, and PM-200). The other input parameters were maintained constant, as listed in Table 4.

The results of the sensitivity analysis for the three surfaces are presented in Fig. 10, where the calculated HTC (Fig. 10a) and maximum subcooling value for sustaining pure DWC (Fig. 10b) are plotted versus the nucleation sites density. Compared to the predictions obtained for the reference $N_s = 2 \times 10^{12}$ m^{-2}, the HTC increases by about 7 % on all the surfaces when N_s is increased by one order of magnitude, while it decreases by 12 % when decreasing N_s down to 2×10^{11} m^{-2}. These variations of q are reflected with similar weights on the predicted maximum ΔT_{max} for promoting pure DWC. In particular, for a N_s increase by an order of magnitude compared to the reference value, the maximum surface subcooling before transition is reduced by 7 %, while it increases by about 14 % when N_s decreases by one order of magnitude.

5. Conclusions

Dropwise condensation on hydrophilic surfaces with reduced contact angle hysteresis has recently emerged as a promising strategy to further enhance two-phase heat transfer, potentially resulting in higher HTC compared to traditional DWC on low-wettability surfaces. However, the extent of this enhancement, as well as the limitations of such surfaces to promote stable DWC without transitioning to filmwise condensation, remain poorly understood.

In this work, condensation of pure steam was studied on two hydrophilic coated aluminum vertical samples ($\theta_a \approx 57^\circ$ for MTO-450, $\theta_a \approx 71^\circ$ for MTO-300) that present reduced contact angle hysteresis ($\Delta\theta < 25^\circ$) compared to the untreated aluminum. Heat transfer measurements and video analysis were performed at constant saturation temperature (107 °C) and vapor velocity (3.5 m s^{-1}) while varying the inlet temperature of the cooling water in the range 20–95 °C, and thus the surface subcooling. The results were also compared to the performance of a sample with lower wettability (PM-200). A summary of the key findings is provided below.

- The results showed that the MTO-450, which displays the highest wettability, exhibited a complete transition from DWC to FWC when increasing the surface subcooling. Pure DWC with roughly constant values of HTC (170 kW m^{-2} K^{-1}) was obtained when $\Delta T_{sub} < 2$. For $\Delta T_{sub} > 25$ K, FWC occurs on the surface leading to HTC values lower than 20 kW m^{-2} K^{-1}. For intermediate ΔT_{sub}, a progressive transition from DWC to FWC was observed, with the formation of elongated droplets and rivulets first, and then the gradual flooding of the surface starting from the bottom.
- The effect of wettability on the DWC/FWC transition was studied by comparing the results obtained on the MTO-450 sample with those over the MTO-300 and PM-200 specimens. In the case of the MTO-300 sample, for $\Delta T_{sub} < 5$ K, the HTC remained almost constant to about 130 kW m^{-2} K^{-1} (pure DWC). For higher values of ΔT_{sub}, the HTC decreases as the condensation mode varied from pure DWC to DWC with elongated drops and short rivulets. Finally, the PM-200 sample sustained pure DWC across the entire ΔT_{sub} range, achieving constant HTCs of about 100 kW m^{-2} K^{-1}. For both the PM-200 and MTO-300 samples, the flooding of the surface was not observed in the whole range of subcooling conditions that can be investigated in the present test rig.
- A comprehensive numerical method developed to predict, for hydrophilic surfaces, the steady-state heat flux (and HTC) during steam DWC and the range of surface subcooling over which pure DWC can be achieved was presented and compared against the present database. The proposed calculation method provides an accurate prediction (within 12 %) of the effect of surface wettability and surface subcooling on the HTC values realized during DWC. Furthermore, it was able to predict the maximum surface subcooling up to which the HTC remains constant (pure DWC).
- Overall, the results indicate that the promotion of DWC on hydrophilic surfaces is possible if the droplet mobility is sufficiently high (i.e. reduced contact angle hysteresis) and the condensation rate is sufficiently low. Furthermore, the higher the surface wettability, the higher the HTC during DWC (due to the lower conduction thermal resistance inside the droplets). Finally, the transition from DWC to FWC occurs at lower subcooling and heat flux over a more hydrophilic surface.

CRediT authorship contribution statement

Marco Tancon: Writing – review & editing, Writing – original draft, Validation, Methodology, Investigation, Formal analysis, Conceptualization. **Antonio Abbatecola:** Writing – original draft, Visualization, Investigation, Formal analysis, Data curation. **Stefano Bortolin:** Writing – review & editing, Supervision, Methodology, Funding acquisition. **Lorenzo Facco:** Resources, Formal analysis. **Riccardo Parin:** Writing – review & editing, Supervision, Formal analysis, Conceptualization. **Davide Del Col:** Writing – review & editing, Supervision, Resources, Project administration, Funding acquisition.

Declaration of competing interest

The authors declare the following financial interests/personal relationships which may be considered as potential competing interests: Stefano Bortolin reports financial support was provided by European Union – Next Generation EU, Mission 4, Component 2 and Italian Ministry for University and Research (MUR) through the project PRIN 2022 WADERE "Development of thermally-driven sorption process for WAtER DEsAlinAtion using low-grade REnEWAblE EnERgy" (CUP C53D23001790006, project code 2022PSPA8R). If there are other authors, they declare that they have no known competing financial interests or personal relationships that could have appeared to influence the work reported in this paper.

Acknowledgements

Financial support of European Union - Next Generation EU, Mission 4, Component 2 and Italian Ministry for University and Research (MUR) through the project PRIN 2022 WADERE "Development of thermally-driven sorption process for WAtER DEsAlinAtion using low-grade REnEWAblE EnERgy" (CUP C53D23001790006, project code 2022PSPA8R) is gratefully acknowledged.

Data availability

Data will be made available on request.

References

[1] B. El Fil, G. Kini, S. Garimella, A review of dropwise condensation: theory, modeling, experiments, and applications, Int. J. Heat Mass Transf. 160 (2020), https://doi.org/10.1016/j.ijheatmasstransfer.2020.120172.

[2] M. Basso, E. Colusso, M. Tancon, S. Bortolin, M. Mirafiori, M. Guglielmi, D. Del Col, A. Martucci, Hydrophobic hybrid silica sol-gel coating on aluminium: stability evaluation during saturated vapour condensation, J. Non-Crystalline Solids X 17 (2023) 100143, https://doi.org/10.1016/J.NOCX.2022.100143.

[3] R. Enright, N. Miljkovic, J.L. Alvarado, K. Kim, J.W. Rose, Dropwise condensation on micro-and nanostructured surfaces, Nanoscale Microscale Thermophys. Eng. 18 (2014) 223–250, https://doi.org/10.1080/15567265.2013.862889.

[4] J.W. Rose, Dropwise condensation theory and experiment: a review, Proc. Inst. Mech. Eng. Part A J. Power Energy 216 (2002) 115–128, https://doi.org/10.1243/09576500260049034.

[5] T.E. Huang, Y. Lu, Z. Wei, D. Li, Q.Y. Li, Z. Wang, K. Takahashi, D. Orejon, P. Zhang, Ultrahigh subcooling dropwise condensation heat transfer on slippery liquid-like monolayer grafted surfaces, ACS Appl. Mater. Interfaces 16 (2024) 53285–53298, https://doi.org/10.1021/ACSAMI.4C12220/ASSET/IMAGES/LARGE/AM4C12220_0008.JPEG.

[6] S. Chavan, H. Cha, D. Orejon, K. Nawaz, N. Singla, Y.F. Yeung, D. Park, D.H. Kang, Y. Chang, Y. Takata, N. Miljkovic, Heat transfer through a condensate droplet on hydrophobic and nanostructured superhydrophobic surfaces, Langmuir 32 (2016) 7774–7787, https://doi.org/10.1021/acs.langmuir.6b01903.

[7] K.K. Varanasi, M. Hsu, N. Bhate, W. Yang, T. Deng, Spatial control in the heterogeneous nucleation of water, Appl. Phys. Lett. 95 (2009) 2007–2010, https://doi.org/10.1063/1.3200951.

[8] S. Sett, P. Sokalski, K. Boyina, L. Li, K.F. Rabbi, H. Auby, T. Foulkes, A. Mahvi, G. Barac, L.W. Bolton, N. Miljkovic, Stable dropwise condensation of ethanol and hexane on rationally designed ultrascalable nanostructured lubricant-infused surfaces, Nano Lett. 19 (2019) 5287–5296, https://doi.org/10.1021/acs.nanolett.9b01754.

[9] S. Bortolin, M. Tancon, D. Del Col, Heat transfer enhancement during dropwise condensation over wettability-controlled surfaces, Surf. Wettability Eff. Phase Chang. (2022) 29–67, https://doi.org/10.1007/978-3-030-82992-6_3.

[10] H. Cha, H. Vahabi, A. Wu, S. Chavan, M.K. Kim, S. Sett, S.A. Bosch, W. Wang, A. K. Kota, N. Miljkovic, Dropwise condensation on solid hydrophilic surfaces, Sci. Adv. 6 (2020), https://doi.org/10.1126/sciadv.aax0746.

[11] E. Colusso, M. Tancon, L. Cazzola, R. Parin, S. Agnoli, F. De Boni, M.G. Pelizzo, E. Della Gaspera, D. Del Col, A. Martucci, Solution-processed graphene oxide coatings for enhanced heat transfer during dropwise condensation of steam, Nano Sel. 2 (2021) 61–71, https://doi.org/10.1002/nano.202000105.

[12] D.J. Preston, Z. Lu, Y. Song, Y. Zhao, K.L. Wilke, D.S. Antao, M. Louis, E.N. Wang, Heat transfer enhancement during water and hydrocarbon condensation on lubricant infused surfaces, Sci. Rep. 81 (8) (2018) 1–9, https://doi.org/10.1038/s41598-017-18955-x.

[13] S.A. Stylianou, J.W. Rose, Drop-to-filmwise condensation transition: heat transfer measurements for ethanediol, Int. J. Heat Mass Transf. 26 (1983) 747–760, https://doi.org/10.1016/0017-9310(83)90026-1.

[14] Y. Utaka, A. Saito, H. Ishikawa, H. Yanagida, Study on dropwise condensation curves (dropwise to filmwise transition of propylene glycol, ethylene glycol and glycerol vapors on a copper surface using a monolayer type promoter - Part 1), Bull. JSME 29 (1986) 4228–4234.

[15] Y. Utaka, A. Saito, H. Ishikawa, H. Yanagida, Study on dropwise condensation curves (dropwise to filmwise transition of propylene glycol, ethylene glycol and glycerol vapors on a copper surface using a monolayer type promoter - Part 2), JSME Int. J. 31 (1988) 73–80.

[16] U. Yoshio, S. Akio, Y. Hiroyuki, On the mechanism determining the transition mode from dropwise to film condensation, Int. J. Heat Mass Transf. 31 (1988) 1113–1120, https://doi.org/10.1016/0017-9310(88)90099-3.

[17] X. Li, P. Cheng, Lattice Boltzmann simulations for transition from dropwise to filmwise condensation on hydrophobic surfaces with hydrophilic spots, Int. J. Heat Mass Transf. 110 (2017) 710–722, https://doi.org/10.1016/j.ijheatmasstransfer.2017.03.033.

[18] Y. Utaka, A. Saito, T. Tani, H. Shibuya, K. Katayama, Study on dropwise condensation curves: measurement of propylene glycol vapor on PTFE coated surface, Bull. JSME 28 (1985) 1150–1157, https://doi.org/10.1299/jsme1958.28.1150.

[19] D. Li, A.W. Neumann, Contact angles on hydrophobic solid surfaces and their interpretation, J. Colloid Interface Sci. 148 (1992) 190–200, https://doi.org/10.1016/0021-9797(92)90127-8.

[20] T. Takeyama, S. Shimizu, On the transition of dropwise-film condensation, in: Proc. 5th Int. Heat Transf. Conf., Tokyo, Japan, 1974, pp. 274–278. https://doi.org/10.1615/ihtc5.1150.

[21] T.S. Thukral, S. Khodakarami, W. Yang, G. Arissi, P. Kabirzadeh, C. Wang, D. Ghaddar, M.J. Hoque, M.A. Pitschman, P.M. Fourspring, N. Miljkovic, Enhancement versus practicality in steam condensation heat transfer, Joule 9 (2025) 101912, https://doi.org/10.1016/J.JOULE.2025.101912.

[22] D. Orejon, J. Oh, D.J. Preston, X. Yan, S. Sett, Y. Takata, N. Miljkovic, K. Sefiane, Ambient-mediated wetting on smooth surfaces, Adv. Colloid Interface Sci. 324 (2024) 103075, https://doi.org/10.1016/J.CIS.2023.103075.

[23] D. Del Col, R. Parin, A. Bisetto, S. Bortolin, A. Martucci, Film condensation of steam flowing on a hydrophobic surface, Int. J. Heat Mass Transf. 107 (2017) 307–318, https://doi.org/10.1016/j.ijheatmasstransfer.2016.10.092.

[24] M. Tancon, R. Parin, S. Bortolin, A. Martucci, D. Del Col, Effect of steam velocity during dropwise condensation, Int. J. Heat Mass Transf. 165 (2021) 120624, https://doi.org/10.1016/j.ijheatmasstransfer.2020.120624.

[25] M. Tancon, A. Abbatecola, M. Mirafiori, S. Bortolin, E. Colusso, A. Martucci, D. Del Col, Investigation of surface inclination effect during dropwise condensation of flowing saturated steam, Int. J. Therm. Sci. 196 (2024) 108738, https://doi.org/10.1016/J.IJTHERMALSCI.2023.108738.

[26] M. Tancon, M. Mirafiori, S. Bortolin, M. Basso, E. Colusso, D. Del Col, Dropwise condensation mechanisms when varying vapor velocity, Appl. Therm. Eng. 216 (2022) 119021, https://doi.org/10.1016/J.APPLTHERMALENG.2022.119021.

[27] M. Tancon, M. Mirafiori, S. Bortolin, M. Basso, E. Colusso, A. Martucci, D. Del Col, Vapor velocity and droplet dynamics during dropwise condensation of steam flowing over hydrophilic surfaces, in: Int. Heat Transf. Conf., Begellhouse, Connecticut, 2023, p. 10, https://doi.org/10.1615/ihtc17.60-70.

[28] A. Bisetto, S. Bortolin, D. Del Col, Experimental analysis of steam condensation over conventional and superhydrophilic vertical surfaces, Exp. Therm. Fluid Sci. 68 (2015) 216–227, https://doi.org/10.1016/j.expthermflusci.2015.04.019.

[29] R. Parin, M. Tancon, M. Mirafiori, S. Bortolin, L. Moro, L. Zago, F. Carraro, A. Martucci, D. Del Col, Heat transfer and droplet population during dropwise condensation on high durability coatings, Appl. Therm. Eng. 179 (2020) 115718, https://doi.org/10.1016/j.applthermaleng.2020.115718.

[30] A. Katselas, R. Parin, C. Neto, Quantification of nucleation site density as a function of surface wettability on smooth surfaces, Adv. Mater. Interfaces (2022) 2200246, https://doi.org/10.1002/ADMI.202200246.

[31] S. Kim, K.J. Kim, Dropwise condensation modeling suitable for superhydrophobic surfaces, J. Heat Transfer 133 (2011) 1–8, https://doi.org/10.1115/1.4003742.

[32] Ł. Chrobak, D. Korte, H. Budasheva, M. Maliński, P. Rodič, I. Milošev, S. Janta-Lipińska, Investigations of the thermal parameters of hybrid sol–gel coatings using nondestructive photothermal techniques, Energies 15 (2022), https://doi.org/10.3390/en15114122.

[33] M. Mirafiori, M. Tancon, S. Bortolin, D. Del Col, Modeling of growth and dynamics of droplets during dropwise condensation of steam, Int. J. Heat Mass Transf. 222 (2024) 125109, https://doi.org/10.1016/j.ijheatmasstransfer.2023.125109.

[34] M. Mei, F. Hu, C. Han, Ergodic simulation of droplet growth during dropwise condensation, Appl. Therm. Eng. 236 (2024) 121929, https://doi.org/10.1016/J.APPLTHERMALENG.2023.121929.

[35] M. Tancon, M. Mirafiori, S. Bortolin, R. Parin, E. Colusso, A. Martucci, D. Del Col, Simultaneous measurement of heat flux and droplet population during dropwise condensation from humid air flowing on a vertical surface, Exp. Therm. Fluid Sci. 136 (2022) 110677, https://doi.org/10.1016/j.expthermflusci.2022.110677.

[36] E.J. Le Fevre, J.W. Rose, A theory of heat transfer by dropwise condensation, in: Proceeding Int. Heat Transf. Conf. 3, Begellhouse, Connecticut, 1966, pp. 362–375. https://doi.org/10.1615/IHTC3.180.

[37] V.P. Carey, Liquid-vapor phase-change phenomena: an Introduction to the Thermophysics of Vaporization and Condensation Processes in Heat transfer Equipment, Hemisphere Pub. Corp., Washington, D.C., 1992.

[38] N. Miljkovic, R. Enright, E.N. Wang, Modeling and optimization of superhydrophobic condensation, J. Heat Transfer 135 (2013) 111004, https://doi.org/10.1115/1.4024597.

[39] A. Abbatecola, M. Tancon, S. Bortolin, D. Del Col, Drag effect of steam flow on droplet removal during dropwise condensation at different surface inclinations,

J. Phys. Conf. Ser. 2766 (2024) 012133, https://doi.org/10.1088/1742-6596/2766/1/012133.

[40] W.H. Wu, J.R. Maa, On the heat transfer in dropwise condensation, Chem. Eng. J. 12 (1976) 225–231.

[41] J. Lethuillier, P. Lavieille, F. Topin, M. Miscevic, About phenomenology and modeling of dropwise condensation, The Surface Wettability Effect on Phase Change (2022) 69–104.

[42] P. Birbarah, S. Chavan, N. Miljkovic, Numerical simulation of jumping droplet condensation, Langmuir 35 (2019) 10309–10321, https://doi.org/10.1021/acs.langmuir.9b01253.

[43] M. Mirafiori, M. Tancon, S. Bortolin, D. Del Col, A new validated model of dropwise condensation of vapor in humid air flow, Int. Commun. Heat Mass Transf. 158 (2024) 107905, https://doi.org/10.1016/J.ICHEATMASSTRANSFER.2024.107905.

[44] J. Lethuillier, M. Miscevic, P. Lavieille, S. Blanco, C. Coustet, F. Topin, Comprehensive correlation for the prediction of the heat transfer through a single droplet in dropwise condensation regime, Appl. Therm. Eng. 209 (2022) 118233, https://doi.org/10.1016/j.applthermaleng.2022.118233.

[45] T. Kim, S.J. Kim, Vertical length effect on dropwise condensation heat transfer at low heat flux – Part II: theoretical model suitable for non-coated metal surfaces, Int. J. Heat Mass Transf. 226 (2024) 125510, https://doi.org/10.1016/J.IJHEATMASSTRANSFER.2024.125510.

[46] N. Suzzi, G. Croce, Numerical simulation of film instability over low wettability surfaces through lubrication theory, Phys. Fluids 31 (2019) 122106, https://doi.org/10.1063/1.5128454/1058957.

[47] C. Yamali, H. Merte, A theory of dropwise condensation at large subcooling including the effect of the sweeping, Heat Mass Transf. Und Stoffuebertragung. 38 (2002) 191–202, https://doi.org/10.1007/S002310100272/METRICS.

[48] F. Wang, M. Zhao, Behavior of moving droplet on inclined containment wall: experiment and model validation, Nucl. Eng. Des. 376 (2021) 111129, https://doi.org/10.1016/J.NUCENGDES.2021.111129.

[49] J.L. McCormick, J.W. Westwater, Nucleation sites for dropwise condensation, Chem. Eng. Sci. 20 (1965) 1021–1036, https://doi.org/10.1016/0009-2509(65)80104-X.

[50] C. Graham, P. Griffith, Drop size distributions and heat transfer in dropwise condensation, Int. J. Heat Mass Transf. 16 (1973) 337–346, https://doi.org/10.1016/0017-9310(73)90062-8.

[51] C. Mu, J. Pang, Q. Lu, T. Liu, Effects of surface topography of material on nucleation site density of dropwise condensation, Chem. Eng. Sci. 63 (2008) 874–880, https://doi.org/10.1016/j.ces.2007.10.016.

[52] I. Tanasawa, J.W. Westwater, What we don't know about the mechanism of dropwise condensation, Int. Heat Transf. Conf. 5 (2019) 186–191, https://doi.org/10.1615/ihtc5.3910.